



Atomistic simulation of the generation of vacancies in rapid crystallization of metals



Miao He^{a,1}, Eaman T. Karim^{b,1}, Maxim V. Shugaev^a, Leonid V. Zhigilei^{a,*}

^a Department of Materials Science and Engineering, University of Virginia, 395 McCormick Road, Charlottesville, Virginia 22904, USA

^b American Dental Association Science and Research Institute, 100 Bureau Drive, Gaithersburg, Maryland 20899, USA

ARTICLE INFO

Article history:

Received 23 August 2020

Revised 2 November 2020

Accepted 2 November 2020

Available online 6 November 2020

ABSTRACT

The generation of vacancies at a crystal-liquid interface propagating under conditions of undercooling below the equilibrium melting temperature is investigated in molecular dynamics simulations performed under well-controlled temperature and pressure conditions for two representative metals, bcc Cr and fcc Ni. The results of the simulations reveal that, for both metals, vacancy concentrations produced in the course of the steady-state propagation of crystallization fronts can exceed the equilibrium values at the corresponding temperatures by orders of magnitude. Different trends in the temperature dependences of vacancy concentration observed for the two metals, namely, the continuous increase with increasing undercooling in Ni and a nonmonotonous temperature dependence in Cr, are related to the qualitatively different temperature dependences of the crystallization front velocity predicted for the two metals. The general character of the computational predictions is confirmed in simulations performed for Ni with four different interatomic potentials and for both metals with (001), (011), and (111) interface orientations. A detailed analysis of atomic rearrangements at the crystallization front suggests that the level of vacancy supersaturation is largely defined by the ability of atoms to migrate within the interfacial region and to fill the numerous vacant sites produced through the simultaneous construction of several atomic crystal planes within the interfacial region. While the majority of the transient vacancies generated during the construction of the crystal planes are annihilated by the atomic flux coming from the liquid side of the interface, a small fraction of the vacancies are trapped behind the crystallization front. Under conditions of strong undercooling, the fast movement of the interface and decreased vacancy mobility prevent the equilibration of vacancy concentration in the newly built crystalline region, thus creating a strong vacancy supersaturation. Analysis of the temperature dependence of the atomic rearrangements occurring at the crystallization front suggests incomplete relaxation of the disordered phase at and in front of the crystal-liquid interface rapidly advancing under conditions of strong undercooling.

© 2020 Acta Materialia Inc. Published by Elsevier Ltd. All rights reserved.

1. Introduction

Rapid crystallization of metals under conditions of deep undercooling below the equilibrium melting temperature is a process of general fundamental importance in materials science as well as of direct practical relevance for a variety of material applications, ranging from high energy particle bombardment [1–5] to short pulse laser processing [6–11] and additive manufacturing [12]. Ultrashort time and high degree of localization of energy deposition, achieved within an electronically excited ion track [13] or a thin

surface layer of a target irradiated by a femtosecond or picosecond laser pulse [14], can produce very steep temperature gradients and cooling rates reaching the levels of $\sim 10^{11}$ – 10^{13} K/s [6–10,15,16]. Resolidification of a transiently melted material can be kinetically inhibited under conditions of such extreme quenching, thus bringing the molten material into a state of deep undercooling or even an amorphous state.

The question on the kinetics of crystallization under conditions of deep undercooling, beyond the regime of linear dependence of the crystallization front velocity on temperature, has been targeted in a number of short pulse laser pump-probe experiments [16–19] suggesting that the crystallization front velocity in pure metals can approach [16] or even exceed [17] 100 m/s at laser fluences close to the surface melting threshold, when the whole melt-

* Corresponding author

E-mail address: lz2n@virginia.edu (L.V. Zhigilei).

¹ Miao He and Eaman T. Karim contributed equally to this work

ing and resolidification process is completed on sub-nanosecond timescale [16–19]. While the direct measurement of the degree of undercooling is not possible in these experiments, the estimations based on solution of heat transfer equation [7,10,16] and the results of molecular dynamics (MD) simulations [7,15,20,21] suggest that the surface of the irradiated target can be undercooled down to 0.9–0.6 T_m by the end of the solidification process, where T_m is the equilibrium melting temperature of the material.

The solidification occurring under conditions of deep undercooling can be expected to yield highly nonequilibrium defect configurations that could affect the radiation damage accumulation [1–5] or define the physical, chemical, and mechanical properties of surface layers modified by short pulse laser irradiation [22]. Indeed, detailed characterization of microstructural changes produced by short-pulse laser irradiation has revealed the presence of high densities of dislocations [23–25], nanoscale twinned domains [7,26], and nanograins [26] in the surface regions of the irradiated targets. The generation of crystal defects has been investigated in large-scale atomistic simulations, which provide insights into the mechanisms responsible for surface nanocrystallization [15,27,28], growth twinning [7], and emission of dislocations [29–31] observed in the experiments.

One intriguing prediction of the simulations, which still awaits experimental confirmation, is the generation of high vacancy concentrations significantly exceeding the equilibrium levels [21,29–34]. The regions where the strong vacancy supersaturation is observed after the laser processing are also the regions that have experienced transient laser-induced melting and resolidification, thus suggesting that the generation of vacancies is related to the crystallization process. Indeed, the results of recent simulations performed for Ni and Ni-Fe/Cr solid solution alloys [34] suggest a direct correlation between the concentration of vacancies and the velocity of crystallization front propagating under conditions of undercooling below T_m . The generation of high concentration of vacancies in the course of rapid far-from-equilibrium crystallization has important practical implications. In particular, the localized melting along ion tracks in materials exposed to energetic ion bombardment can result in the generation and clustering of point defects, leading to the radiation damage accumulation [2–5]. The defect generation in melting and resolidification caused by short laser pulse irradiation may produce the so-called incubation effect, when the laser fluence threshold for ablation/damage decreases with increasing number of laser pulses [35–37]. In multi-component systems, the large number of vacancies may also foster atomic diffusion and play an important role in redistribution of impurities, mixing/alloying, or chemical ordering.

In this paper, we perform a detailed analysis of the mechanisms of vacancy generation at the crystallization front propagating under well-controlled undercooling conditions. The analysis is based on the results of MD simulations performed for two representative metals, body centered cubic (bcc) Cr and face centered cubic (fcc) Ni, a broad range of undercooling conditions extending down to temperatures where the solid-liquid interface ceases to move, and different crystallographic orientations of the crystallization front. The correlations between the velocity of solid-liquid interface and the concentration of vacancies trapped behind the crystallization front is established and related to the atomic-scale mechanisms of crystallization. The sensitivity of the results to the interatomic interaction potential is also investigated by comparing the results obtained with four different potentials for Ni. The computational setup used in the MD simulations of the crystallization process is briefly described in Section 2, the results are reported and discussed in Section 3, and the conclusions on the vacancy generation mechanisms and their connection to the crystallization kinetics are provided in Section 4.

2. Computational setup

In order to identify the general mechanisms responsible for the generation of vacancies in the course of rapid solidification, several series of MD simulations are performed for bcc Cr and fcc Ni crystal-liquid coexistence systems, where the steady propagation of crystallization fronts proceeds under well-controlled undercooling conditions. The coexistence systems represent solid slabs surrounded by molten material. The lateral sizes of the computational systems, in the directions parallel to the crystal-liquid interfaces, are chosen so that the lattice parameters in the crystalline parts are equal to the equilibrium values at a desired temperature and zero pressure. The liquid part is prepared by superheating a crystalline material to 1.3–2.0 T_m to induce rapid homogeneous melting [38,39], followed by cooling of the molten part down to the desired temperature. The periodic boundary conditions are applied in all directions, and a constant zero pressure is maintained by scaling the system in the direction of the longest axis normal to the crystal-liquid interfaces using the Berendsen barostat algorithm [40].

To avoid local temperature spikes near the advancing crystallization fronts due to the release of latent heat of melting [27,34,41], the computational systems are divided into slices with thickness of 2–4 nm parallel to the crystal-liquid interfaces, and the temperature is controlled through the Berendsen thermostat algorithm [40] applied independently to each slice. We note that the formation of a temperature spike at a rapidly advancing solidification front is a real effect that should be taken into account when comparing the results of the simulations reported in this paper to experimental data [16]. In metals, where the electrons make the dominant contribution to the heat transfer, the actual vibrational (phonon) temperature at a rapidly advancing crystallization front is defined by the kinetic balance between the release of the latent heat of melting upon the crystallization, the electron-phonon energy transfer at the interface, and the electron heat conduction from the crystal-liquid interface to the surrounding colder material. The finite time of electron-phonon equilibration can create a gap between the electron and phonon temperatures in the interfacial region. Computationally, the conditions of electron-phonon nonequilibrium generated at a rapidly propagating melting [42] or crystallization [10,15,16,21,27,34] fronts can be accounted for with the two-temperature model (TTM) [43] or a combined TTM-MD approach [44]. Since the kinetics of the liquid-crystal interface is controlled by the local phonon temperature of the interfacial region, the results of the present study can be readily mapped to the conditions predicted in TTM or TTM-MD simulations.

The interatomic interactions in the Cr system are described by the embedded atom method (EAM) potential with parameters suggested in Ref. [21]. To investigate the effect of interatomic potential on the generation of vacancies, the simulations for Ni are performed with four EAM potentials suggested by Johnson [45], Foiles, Baskes, and Daw (FBD) [46], Mishin [47], and Bonny [48], respectively. For all the potentials, the equilibrium melting temperatures are determined in series of crystal-liquid coexistence simulations performed under well-controlled temperature and zero pressure conditions. For EAM Cr, the melting temperature of 2366 K, is within 1% of the value reported for the same potential by Lin *et al.* [21] and is 9% above the experimental value of 2180 K [49]. The melting temperatures calculated for Johnson, FBD, Mishin, and Bonny EAM Ni potentials are 1445 K, 1719 K, 1701 K [50], and 1530 K [34], respectively, with all the values being lower than the experimental value of 1728 K [49]. The effect of crystallographic orientation of the crystal-liquid interface on the velocity of the crystallization front and vacancy concentration is investigated by considering systems with (100), (011), and (111) orientations of the interface in Cr and in Mishin's EAM Ni coexistence systems.

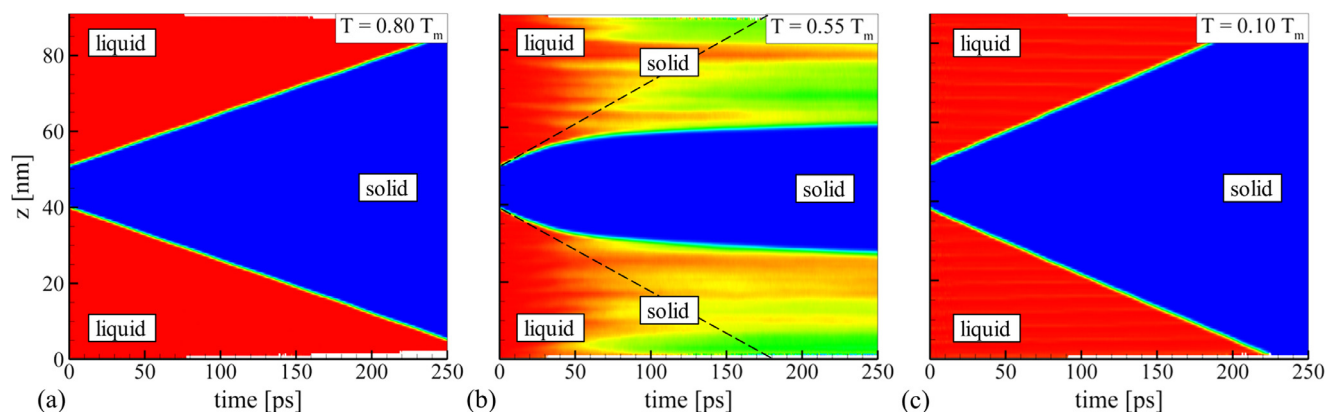


Fig. 1. Contour plots depicting the evolution of the fraction of liquid phase in MD crystal-liquid coexistence simulations performed for the Ni system with lateral size of 28 nm at undercooling levels of $0.8T_m$ (a), $0.55T_m$ (b), and $0.1T_m$ (c). The regions of liquid and solid phases are noted on the plots. The dashed lines in (b) predict the position of the solid-liquid interface in the absence of homogeneous nucleation based on the initial velocity of the crystallization front. The appearance of yellow and green regions in (b) reflect the formation of a nanocrystalline region in the course of homogeneous solidification.

3. Results and discussion

The results of MD simulations of crystallization front propagation are discussed in this section first for Cr and Ni systems represented by Johnson EAM potentials [21,45]. Out of the four EAM potentials used for Ni, this potential predicts the lowest propensity for homogeneous nucleation of new crystallites under conditions of deep undercooling down to $\sim 0.65T_m$ and below (see Appendix A). As a result, it was possible to extend the simulations of the melting front propagation with this potential to the whole range of undercooling temperatures, down to $0.01T_m$. The dependence of the velocity of the crystallization front on the undercooling temperature predicted in the simulations is presented and related to the earlier studies and analytical models in Section 3.1. The vacancy concentration in the solidified part of the system and the mechanisms of the vacancy generation at the crystallization front are discussed in Section 3.2. The sensitivity of the computational predictions to the interatomic potential and crystallographic orientation of the crystal-liquid interface are discussed in Sections 3.3 and 3.4, respectively.

3.1. Velocity of crystallization front

The simulations of crystallization process discussed in this section are performed for temperatures ranging from T_m to $0.1T_m$ for Cr and to $0.01T_m$ for Ni, with the interatomic interactions described by Johnson potential [21,45]. The lateral dimensions of the computational system used for Cr are $17 \times 17 \text{ nm}^2$, while systems of two sizes, $28 \times 28 \text{ nm}^2$ and $5 \times 5 \text{ nm}^2$ are used for Ni. The crystallization front velocities are calculated by tracking the movement of the two liquid-crystal interfaces present in the coexistence systems, as illustrated in Fig. 1. This figure shows the spatial and time evolution of the fraction of liquid phase in three representative simulations performed for a Ni system with lateral size of 28 nm. The interface velocities can be reliably determined from the plots shown in Figs. 1a and 1c, where a steady-state propagation of the crystallization fronts is observed for temperatures of $0.8T_m$ and $0.1T_m$.

In the simulations performed in the range of temperatures from $0.35T_m$ to $0.65T_m$, however, the crystallization process is complicated by the onset of homogeneous nucleation of new crystallites inside the undercooled liquid. This effect is exemplified for a temperature of $0.55T_m$ in Fig. 1b, where the emergence of new regions with nonzero fraction of crystalline atoms can be seen. As discussed in more detail in Appendix A, the homogeneous nucleation of new crystallites results in deceleration of the interface between

the “main” crystal growing from the initial seed and the rest of the system. This deceleration is related to the need for small randomly nucleated crystallites to reorient and join the growing main crystal. The growth of multiple new crystallites may also lead to the formation of a continuous nanocrystalline region, bringing the growth of the main crystal to a halt. The nucleation and growth of new crystallites not only makes it impossible to obtain a reliable estimate of the crystallization front velocity for a particular crystallographic orientation of the crystal-liquid interface, but also complicates the analysis of the vacancy generation, which is the main focus of the present study. In particular, for the Johnson EAM Ni system with 28 nm lateral size, the nucleation starts at $\sim 0.65T_m$, and reliable values of the crystallization front velocity and vacancy concentration cannot be obtained for temperatures below $0.6T_m$. The probability of nucleation of new crystallites at a time scale required for the evaluation of crystallization front velocity in MD simulations can be reduced by decreasing the lateral size of the computational systems. Therefore, we use a system with smaller 5 nm lateral size to extend the simulations to deeper undercooling conditions, below $0.6T_m$. Note that the rate of homogeneous nucleation is sensitive to the parametrization of the EAM potentials [51]. In particular, the analysis reported below, in Section 3.3, indicates that the nucleation predicted with most of the alternative EAM potentials for Ni is more active as compared to Johnson EAM Ni, which limits the range of temperatures where the steady-state crystallization front propagation can be studied to $T > 0.65T_m$.

The crystallization front velocities evaluated in the simulations performed for Johnson EAM Cr and Ni at different levels of undercooling are shown in Fig. 2a,b. For both systems, two distinct temperature regimes can be identified in the kinetics of the crystallization front propagation. In the regime of small to moderate undercooling, extending from the melting temperature T_m down to $\sim 0.75T_m$ for Cr and to $\sim 0.7T_m$ for Ni, the crystallization front velocity increases with decreasing temperature in a similar manner for both metals and reaches its maximum value of $\sim 140 \text{ m/s}$ for Cr and $\sim 170 \text{ m/s}$ for Ni. At lower temperatures, under conditions of deep undercooling, however, the two systems exhibit very different temperature dependences of the crystallization front velocity. In the case of Cr, a steady decrease of the velocity from its maximum value is observed with increasing undercooling, and the velocity drops down to a level that cannot be resolved in an MD simulation at $\sim 0.1T_m$ (no noticeable motion of the interface is recorded during a 10 ns-long simulation at this temperature). In contrast, for Ni, the crystallization front velocity stays at an approximately constant level of 160 – 180 m/s in a broad range of temperatures

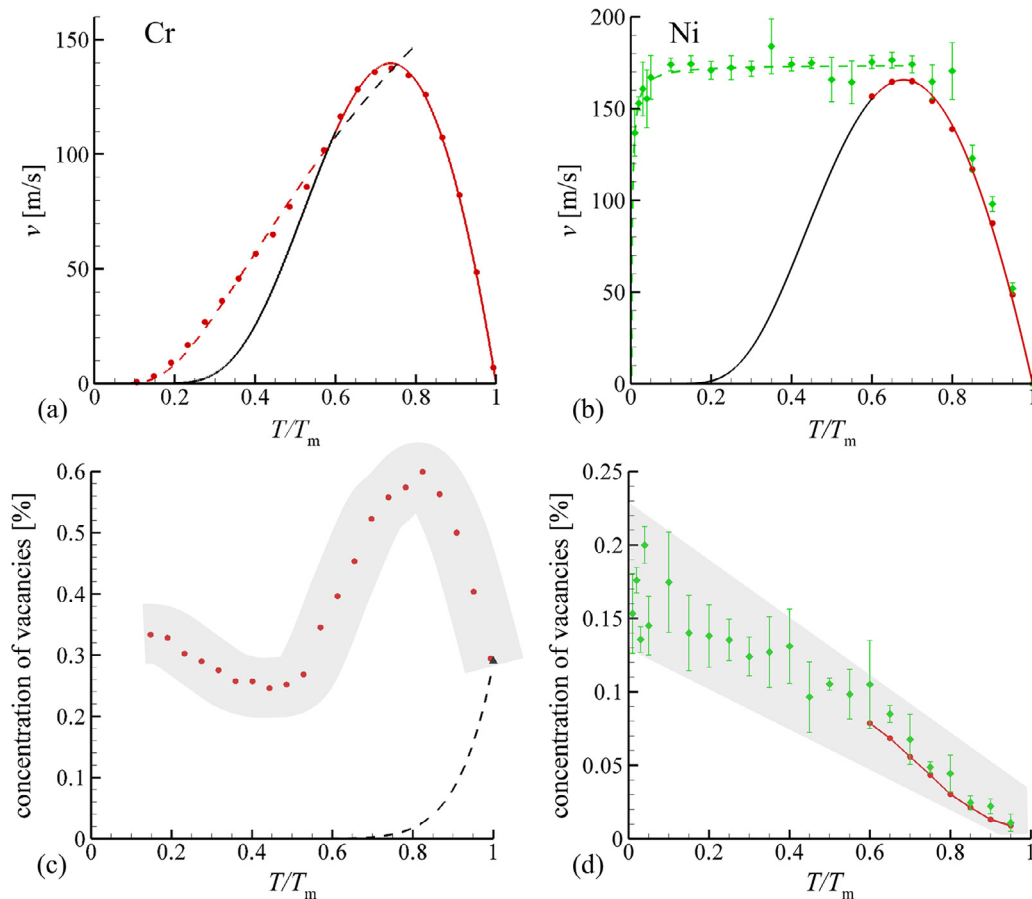


Fig. 2. Velocities of crystallization front and concentrations of vacancies in solidified parts of Cr (a,c) and Ni (b,d) crystal-liquid coexistence systems predicted in MD simulations performed at different levels of undercooling below the equilibrium melting temperature. The red circles represent the results of the simulations performed for larger systems with lateral size of 17 nm for Cr and 28 nm for Ni, while green diamonds show the results for smaller Ni systems with lateral size of 5 nm. For smaller-scale simulations, the error bars represent the standard deviations obtained by rerunning simulations three times for the same undercooling, each starting at different initial conditions. For larger-scale simulations, the error bars are comparable to the size of the symbols representing the data points and are not shown. The solid and dashed lines in (a,b) show the predictions of Eqs. (1) and (2), respectively, with parameters provided in Table 1. The red and green parts of the curves correspond to the temperature range where the equations provide a good description of the MD results, while the parts where the equations do not match the results of the simulations are colored black. The black triangle in (c) is the equilibrium concentration of vacancies at T_m predicted in an MD simulation, and the dashed line shows the theoretical equilibrium concentration of vacancies evaluated as described in Appendix C. The grey areas in (c,d) serve as guidance to the eye and highlight the difference in the dependences of vacancy concentration on undercooling predicted for Cr and Ni.

extending down to $0.05T_m$. Further cooling from $0.05T_m$ to $0.01T_m$ leads to the decreases of the velocity from 167 m/s to 137 m/s.

The temperature dependences of the crystallization front velocity obtained in this work for Cr and Ni are consistent with the results of earlier MD simulations, where extended plateaus of the crystallization front velocity at low temperatures are commonly observed for fcc metals, while a gradual decrease of the velocity from the maximum value down to zero level is reported for most of the bcc metals [52–57]. The exceptions from this general trend have also been reported, e.g., an observation of a plateau extending down to $-0.2T_m$ for bcc Ta [53] and a gradual decrease of the crystal growth velocity reported for fcc Al [57].

The two regimes of the crystal growth cannot be consistently fitted to any single kinetic equation suggested for the description of the crystallization process [58–60], although the traveling wave solution of the phase field model has been shown to provide, with appropriate choice of parameters and an account for the conditions of local nonequilibrium at the crystal-liquid interface, a consistent description of the transition between the low and high temperature regimes observed in MD simulations [61]. In the present study, we follow an approach suggested in Ref. [53], and describe the temperature dependence of the velocity of crystallization front by two independently fitted kinetic equations.

In the temperature range from T_m down to $0.6T_m$, the velocity of the crystallization front is described by the Wilson-Frenkel expression based on the phenomenological transition state theory that considers the exchange of atoms between the liquid and crystal phases at the interface [60],

$$v(T) = v_0^h \exp(-E_a^h/k_B T) [1 - \exp(-\Delta G(T)/k_B T)], \quad (1)$$

where $\Delta G(T)$ is the free energy difference between the liquid and crystal phases, E_a^h is the activation energy associated with the mobility of atoms in the liquid phase, k_B is the Boltzmann constant, and v_0^h is a constant prefactor. At moderate deviations from the equilibrium melting temperature T_m , the temperature dependence of the thermodynamic driving force $\Delta G(T)$ can be approximated as $\Delta G(T) \approx \Delta H_m(T_m - T)/T_m$, where ΔH_m is the latent heat of melting at T_m . While the difference of the heat capacities of the crystal and liquid phases can lead to a deviation of $\Delta G(T)$ from this approximation, the deviation remains relatively small in the range of temperatures where Eq. (1) is fitted to the results of MD simulations in the present study. The values of ΔH_m are determined in a separate set of MD simulations performed for liquid and solid phase EAM Cr ($\Delta H_m = 22.6$ kJ/mol = 0.234 eV/atom)[21] and EAM Ni ($\Delta H_m = 14.47$ kJ/mol = 0.15 eV/atom) [62].

Table 1

The parameters of Eqs. (1) and (2) fitted to describe the dependence of the velocity of (001) crystal-liquid interface on the level of undercooling in the high ($T_m \geq T \geq 0.6T_m$) and low ($T < 0.6T_m$) temperature regions, respectively. The interatomic interactions in Ni and Cr systems are described by Johnson EAM potential [21,45]. The latent heat of melting calculated for this potential is 0.150 eV/atom for Ni and 0.234 eV/atom for Cr.

	v_0^h , m/s	E_a^h , eV	v_0^l , m/s	E_a^l , eV
Ni	3848	0.195	174	0.320×10^{-3}
Cr	9066	0.464	384	0.156

The two parameters of Eq. (1), E_a^h and v_0^h , obtained by fitting to the results of MD simulations in the range of temperatures from T_m to $0.6T_m$, are listed in Table 1. As can be seen from Fig. 2a,b, Eq. (1) provides an adequate description of the MD results in this range of temperatures, including the nearly linear increase in the close vicinity of T_m , commonly described in terms of the kinetic coefficient [41,60,63–66], weakening of the dependence with increasing undercooling, and transition through a maximum at $\sim 0.75T_m$ for Cr and $\sim 0.7T_m$ for Ni. This behavior is characteristic of the diffusion-controlled crystallization process described by Eq. (1), where the increase of the crystal-liquid interface velocity in the vicinity of T_m is defined by the increase in the thermodynamic driving force for the phase transformation, $\Delta G(T)$, while the decrease in atomic mobility with increasing undercooling, accounted for by $\exp(-E_a^h/k_B T)$ in Eq. (1), drives the velocity through the maximum and into a gradual decrease at lower temperatures.

The decrease of the crystallization front velocity with further increase of the undercooling predicted in MD simulations, however, is substantially weaker than that predicted by Eq. (1) for Cr, and is virtually absent in a broad range of temperatures for Ni. The inability of Eq. (1) to provide an adequate description of the MD results is apparent from the large deviation between the data points and parts of the solid lines colored black in Fig. 2a,b. Nominally, the temperature dependence of the interface velocity predicted in MD simulations at $T < 0.6T_m$ can be described by a simple Arrhenius equation,

$$v(T) = v_0^l \exp(-E_a^l/k_B T), \quad (2)$$

with the values of the two fitting parameters listed in Table 1. The activation energy E_a^l produced by fitting to the MD results, however, is reduced by almost a factor of 3 with respect to the activation energy E_a^h found for the higher temperature regime for Cr. For Ni, the apparent activation energy required to describe the extended plateau in the temperature dependence of the crystallization front velocity (Fig. 2b) by Eq. (2) is close to zero, suggesting an athermal character of the crystallization process [53].

Note that the transition to the region with weaker temperature dependence of the crystallization front velocity is observed at the levels of undercooling approaching the glass transition temperature T_g . For the EAM Cr, $T_g = 810 \text{ K} = 0.35T_m$ is determined [33] from the temperature dependence of the second moment of the atomic-level hydrostatic stress distribution, following a method suggested in Ref. [67]. For the EAM Ni, $T_g = 717 \text{ K} = 0.5T_m$ is found [8] from the temperature dependence of the shape of the pair distribution function, using a criterion suggested in Ref. [68]. The range of temperatures where the crystal growth velocity is increased and the apparent activation energy is greatly reduced with respect to the diffusion-controlled growth ($E_a^l \ll E_a^h$), therefore, corresponds to the transition from crystal-liquid to crystal-glass interfacial kinetics. While, at a general level, the drastic drop in the apparent activation energy in bcc Cr and the transition to the athermal crystallization kinetics in fcc Ni at $T \leq T_g$ can be attributed to

the limited relaxation of glass or deeply undercooled liquid in the vicinity of the advancing crystallization front [53,61,69], a reliable predictive analytical model of crystallization front propagation in the absence of full relaxation of the disordered phase is still lacking for this regime.

The direct quantitative experimental verification of the values of crystallization front velocity predicted in MD simulations for the conditions of deep undercooling is not feasible, although the results of time-resolved probing of resolidification in metal targets irradiated by short laser pulses [16–19] are consistent with maximum crystallization front velocities on the order of 100 m/s. *Ex situ* analysis of the microstructure of laser-processed samples can also reveal the signs of deep undercooling realized in the course of solidification. In particular, the observation of nanoscale horizontal twinned domains in subsurface regions of single crystal Ni targets with (111) surface orientation suggests a highly nonequilibrium character of the solidification process, as the growth twinning is predicted to only occur at $T < 0.87T_m$ [7]. Finally, the difference in the crystal growth kinetics in bcc and fcc metals illustrated by Fig. 2a,b may be related to the inability to produce stable one-component metallic glass from fcc metals even at extreme cooling rates of $\sim 10^{13} \text{ K/s}$ realized in a specially designed experimental setup [55]. The thermal stability of the amorphous tantalum and vanadium produced in this study through the ultra-rapid quenching may be explained by the crystal growth rate vanishing with decreasing temperature for bcc metals (e.g., Fig. 2a), while for fcc metals the velocity of the crystallization front remains high even at extreme levels of undercooling (e.g., Fig. 2b).

3.2. Generation of vacancies at crystallization front

Following the complete resolidification of the crystal-liquid coexistence systems, the final computational samples are quenched to zero temperature and analyzed to identify the vacancies produced in the crystallization process. The regions that belong to the initial crystal, the parts of the system crystallized during the preparation of the coexistence system at a desired temperature, the regions where the two solidification fronts meet each other creating high density of crystal defects, and the regions solidified through the homogeneous nucleation of new crystallites are all excluded from the analysis of the vacancy concentration. Only the parts of the system where the crystallization proceeded through the steady-state propagation of crystal-liquid interfaces are used in the calculation of vacancy concentration defined as the average fraction of unoccupied lattice sites in the crystalline planes present in the regions of interest.

The results of the calculation of the vacancy concentration at different levels of undercooling are shown for the Cr and Ni systems in Fig. 2c,d. In the Cr system, the vacancy concentration increases with decreasing temperature from 0.29% at $0.99T_m$ to the maximum level of 0.60% at $0.82T_m$. This increase is followed by a sharp drop down to 0.27% at around $0.53T_m$ and a moderate rise up to 0.33% at $0.15T_m$, which is the lowest temperature when a noticeable movement of the solidification front is observed. In contrast to the nonmonotonous dependence of the vacancy concentration obtained for Cr, the results for the Ni system exhibit a nearly linear increase from a much lower, as compared to Cr, starting level of $9.05 \times 10^{-3}\%$ at $0.95T_m$ to a maximum value of $\sim 0.17\%$ at $0.1T_m$. The qualitative difference in the general trends observed for the temperature dependence of the vacancy concentration in Cr and Ni systems is visually highlighted by the grey shaded areas encompassing the data points in Fig. 2c,d.

Despite the quantitative differences in the values of vacancy concentration and qualitative differences in its temperature dependence, an important computational prediction common for both systems is that the vacancy concentrations generated by the rapid

crystallization are orders of magnitude higher than the equilibrium levels at corresponding temperatures. This prediction is illustrated by adding a dashed line in Fig. 2c showing the temperature dependence of the equilibrium concentration of vacancies calculated for the EAM Cr system as described in Appendix C. At T_m , the equilibrium vacancy concentration, $n_{eq} = 2.9 \times 10^{-3}$, marked in Fig. 2c by the black triangle, is very close to the vacancy concentration generated at the crystal-liquid interface propagating with a velocity of 7 m/s at $T = 0.99T_m$. As the undercooling increases, however, the equilibrium vacancy concentration drops by orders of magnitude, to less than 10^{-4} at $0.76T_m$ and less than 10^{-6} at $0.57T_m$. At the same time, the vacancy concentration generated in the crystallization process remains above 2×10^{-3} at all levels of undercooling, down to $0.15T_m$. We can conclude, therefore, that the crystallization occurring under conditions of strong undercooling below the melting temperature can produce strong vacancy supersaturation exceeding the equilibrium levels of vacancy concentration by many orders of magnitude.

The prediction of the strong vacancy supersaturation produced by the nonequilibrium crystallization process is consistent with the observation of high vacancy concentrations in atomistic simulations of ultrashort pulse laser processing of metals, which involves transient melting and rapid resolidification of thin surface layers of irradiated targets [21,29–34]. In particular, the vacancy concentrations of 0.1% to 0.5% are observed in the surface regions of Cr targets irradiated in vacuum [21,29,30,32,33] and water environment [31], ~0.15% in Ag targets [32], ~0.1% in Ni, ~0.15% in Ni₈₀Fe₂₀, ~0.1% in Ni₈₀Cr₂₀, and ~0.02% in Ni₅₀Fe₅₀ targets [34], with all targets represented by EAM potentials. Due to the strong localization of the laser energy deposition and steep temperature gradients, the cooling of the transiently melted surface regions in short pulse laser processing of metal targets is very rapid, up to $\sim 10^{11}$ – 10^{13} K/s [10], and the levels of undercooling of 0.9 – $0.8T_m$ can readily be achieved prior to the solidification. Similarly high levels of vacancy concentration, up to ~0.3% have also been observed in MD simulations of crystallization performed under controlled temperature conditions for several fcc metals and solid solution binary alloys [33,34,57].

In order to understand the atomic-scale mechanisms responsible for the generation of the high vacancy concentrations in the rapid crystallization process, we perform a detailed analysis of the atomic rearrangements at the advancing crystallization front. The analysis is done for a small (3 nm × 3 nm × 100 nm, 70,000 atoms) Cr crystal-liquid coexistence system with (001) orientation of the two crystal-liquid interfaces. The uniform temperature of $0.57T_m$ is maintained throughout the system as explained in Section 2. The system is divided into 700 layers parallel to the crystal-liquid interfaces, so that each layer in the solid part corresponds to one atomic plane (100 atoms in the absence of crystal defects), and the atoms are assigned identification numbers according to the planes they belong to. A side view of a part of the system in the vicinity of the interface is shown for a time of 102 ps in Fig. 3a, where the atoms are colored according to the plane identification numbers. The top views of four of the planes identified in Fig. 3a are shown in Fig. 3b for six moments of time during the following 9.5 ps, when the crystallization front passes through these planes.

To facilitate the analysis of atomic rearrangements involved in the construction of the bcc crystal lattice at the crystallization front, the atoms that are going to move to another plane by the time the next snapshot is shown for are marked by crosses colored according to the plane of their destination. The atoms that came from a different plane during the time period illustrated in the figure are outlined by circular ribbons with color reflecting the plane of origin. For example, during the time between 102 ps and 104 ps, 8 atoms originally located within plane 240 jumped to plane

239 to occupy the lattice sites within this plane. These atoms are labeled in plane 240 at a time of 102 ps by green crosses, with the green color reflecting their new position within plane 239 at 104 ps. The same 8 atoms appearing in plane 239 starting from 104 ps are encircled by yellow ribbons denoting their origin from plane 240. The atoms that are going to move to and came from planes not shown in Fig. 3b (planes with identification numbers lower than 239 or higher than 242) are marked by black crosses and black ribbons, respectively.

The representation of the rapid atomic rearrangements occurring at the crystallization front provided in Fig. 3b enables a detailed analysis of the vacancy generation mechanisms. At a time of 102 ps, the formation of the ordered crystal structure within plane 239 is almost complete, plane 242 is largely disordered and can be considered to belong to the liquid phase, while planes 240 and 241 can be associated with the interfacial region. During the following 9.5 ps, the crystal structure in the interfacial region gradually builds up through atomic rearrangements leading to the increased occupation of the lattice sites. These rearrangements are irreversible and are stabilized by a large thermodynamic driving force for crystallization, resulting in the advancement of the crystal-liquid interface. Since the liquid phase of metals has lower density and more “open” structure than solid, a large number of vacant lattice sites are formed at the advancing crystallization front. Most of these sites are then filled by atoms jumping from upper planes (higher identification numbers in Fig. 3) in the direction opposite to the crystal growth. The minority of the vacant sites, however, are not filled by atoms jumping from the more disordered liquid side of the interface and are left behind the rapidly advancing crystallization front. These “lucky survivors” are the vacancies observed in the final crystal structures produced by the nonequilibrium crystallization and counted to yield the values of vacancy concentration plotted in Fig. 2c,d.

The scenario described above can be exemplified by considering atomic jumps between the planes shown in Fig. 3b. Let us start the analysis from plane 239, which has 94 atoms (6 vacancies) at a time of 102 ps. During the time period from 102 to 104 ps, 3 atoms from this plane move to plane 238 (marked by black crosses) and annihilate vacancy sites there, and one atom with yellow cross jump to plane 240. During the same time period, 8 atoms from plane 240 and one atom from plane 238 move to plane 239, leaving only one vacancy site in plane 239 at 104 ps. During the following 1.5 ps, 2 atoms move from plane 239 to plane 238, including the atom that came from plane 238 in the previous time period. The resulting 3 vacancy sites are filled by 3 atoms jumping from plane 240, making this plane defect-free. Switching our attention to plane 240, we note that this plane has 97 atoms (equivalent to 3 vacancy sites) at 102 ps. During the following 2 ps, 8 of the atoms from this plane move down to plane 239, while 8 new atoms are joining the plane from the side of the liquid (7 atoms originate from plane 241 and one from plane 242). Three atoms move from plane 240 to plane 241 during the time period of 102 – 104 ps and jump back to plane 240 within the following 1.5 ps, therefore, these atoms are marked by yellow ribbons with crosses in plane 241 at 104 ps. We also notice an atom marked by green ribbon with cross in plane 240 at 104 ps, which jumps back and forth between plane 239 and plane 240 between 102 ps and 105.5 ps. In addition, at the time of 104 ps, two atoms with green crosses are going to leave plane 240 towards plane 239, and three atoms with yellow crosses are going to move to plane 240 from plane 241. The overall atomic flux through plane 240 during the initial 3.5 ps illustrated in Fig. 3b adds only one atom to this plane, but helps to eliminate 10 vacancy sites in the underlying crystalline planes. During the following 3 ps, the two vacancies remaining in plane 240 are eliminated by atoms jumping into this plane from

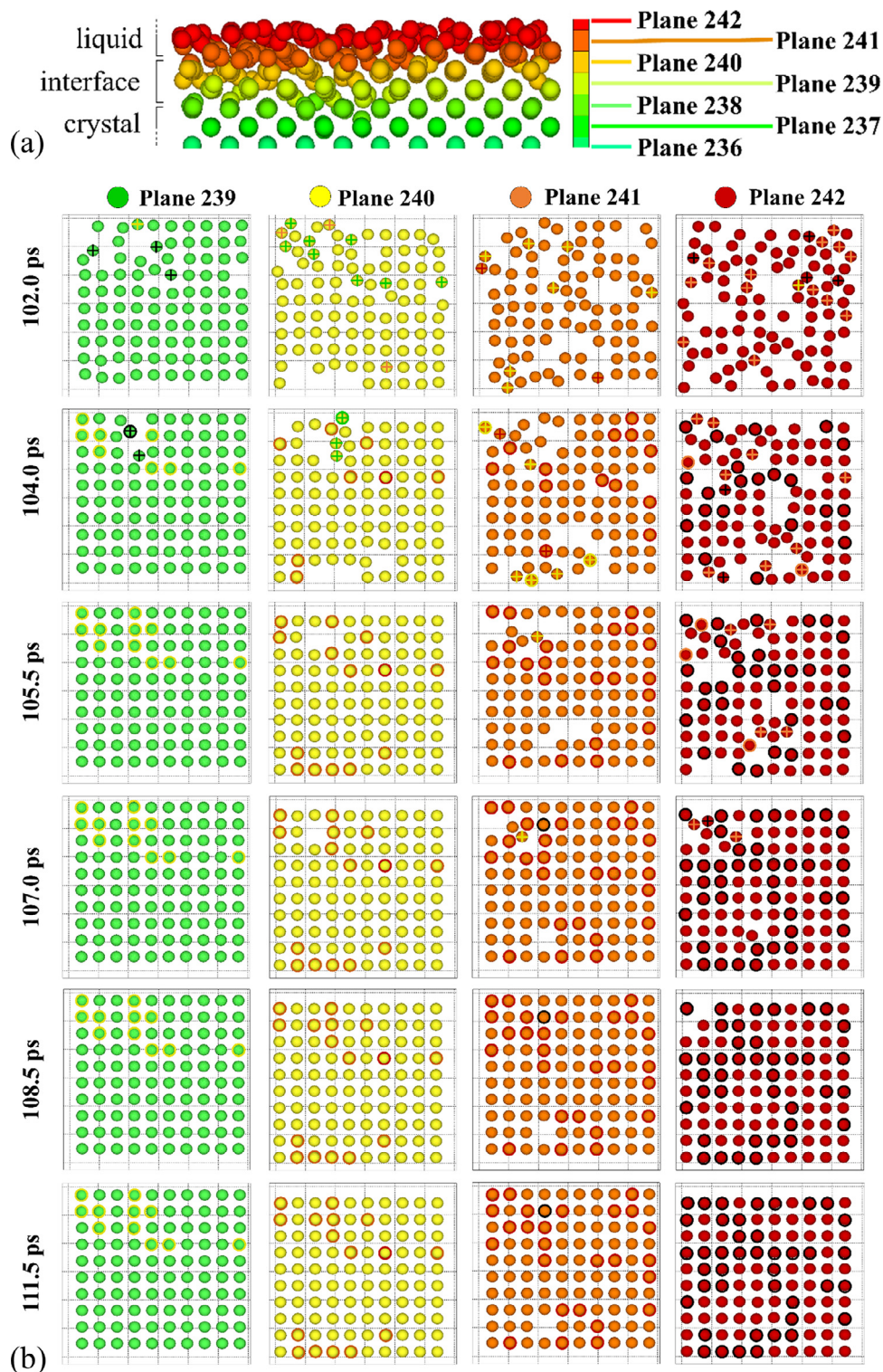


Fig. 3. Close up view of four atomic planes that, at a time of 102 ps, include liquid-like plane 242, interfacial region (planes 241 and 240), and largely crystalline plane 239 in a simulation performed at $T = 0.50T_m$ for a Cr crystal-liquid coexistence system with (001) orientation of crystal-liquid interfaces. The side view of the planes is shown for 102 ps in (a) and the top views of the four planes are shown for six consecutive moments of time in (b). The atoms are colored according to the atomic planes they are associated with. The atoms with circular ribbons are the ones that came from a different plane during the time span illustrated in the figure, and the color of the ribbons corresponds to their plane of origin. The atoms marked by crosses are the ones that are going to move to another atomic plane at the next moment of time shown in the figure, and the color of the crosses represents the color of their new atomic plane. The black ribbons and black crosses indicate that the planes of origin and destination, respectively, are below plane 239 or above plane 242, which are not shown in (b). The atomic configurations are quenched to 0 K in order to reduce the thermal noise in atomic positions.

plane 241, completing a perfect crystalline plane by 108.5 ps. Similar processes of vacancy annihilation are observed for the other two planes (241 and 242) shown in Fig. 3b. A notable difference, however, is that one vacancy in plane 241 is not annihilated and is trapped behind the crystallization front. This vacancy is confirmed to stay in place as the crystallization front moves away from the plane containing the vacancy.

Note that once a vacancy is generated at an advancing crystal-liquid interface, it can hardly escape through diffusion towards the interface rapidly moving away under conditions of deep undercooling below the equilibrium melting temperature. The characteristic time between jumps of a vacancy in the crystal lattice, τ_v , can be estimated from the vacancy jump rate, $1/\tau_v = 6D_v/r_1^2$, where D_v is the diffusion coefficient of a vacancy and r_1 is the nearest neighbor distance in the crystal lattice ($r_1 = \sqrt{3}/4a$ for bcc and $r_1 = a/\sqrt{2}$ for fcc, where a is the lattice parameter). Using the Arrhenius expression for the diffusion coefficient, $D_v(T) = D_v^0 \exp(-E_v^m/k_B T)$ with parameters calculated for EAM Cr in Ref. [21], $E_v^m = 0.81$ eV and $D_v^0 = 0.39 \times 10^{-6}$ m²/s, the characteristic time between vacancy jumps at a temperature used in the simulation illustrated in Fig. 3, $T = 0.5T_m$, is $\tau_v = 76$ ps. With the crystallization front velocity of ~ 80 m/s at this temperature (Fig. 2a), the front moves ~ 6 nm away from the vacancy during time τ_v , i.e., about 42 atomic planes, such as the ones shown in Fig. 3b, are added during the characteristic time of a vacancy jump. Close to the melting temperature, however, the time between vacancy jumps can exceed the time required for the addition of a single crystal lattice plane. In particular, $\tau_v = 1.5$ ps at $0.99T_m$, when the interface velocity is 7 m/s. Thus, a vacancy can jump ~ 14 times during the buildup of a single atomic plane of the crystal lattice. As a result, the vacancy concentration generated at this low level of undercooling is very close to the equilibrium vacancy concentration, as can be seen in Fig. 2c.

The results of the detailed analysis of atomic-level rearrangements at the crystallization front provided above for Cr (001) interface are consistent with the results of a similar analysis performed for the crystal-liquid coexistence Bonny EAM Ni (001) system undergoing crystallization at $0.72T_m$ (not shown). The results obtained for both Cr and Ni suggest the following scenario of the vacancy generation in the far-from-equilibrium crystallization process. The rapid buildup of the crystal lattice proceeds through the simultaneous construction of several atomic planes constituting the interfacial region. Due to the partially disordered structure of the atomic planes within the interfacial region, the number of atoms within the atomic planes tend to be smaller than that of the perfect crystal, and the disordered regions serve as precursors of vacancy sites. Most of the vacancies and vacancy precursors within the interfacial region are rapidly (on the timescale it takes for the interface to propagate a distance comparable to the thickness of the interface, τ_i) annihilated by the flux of atoms coming from the liquid side of the interface. A small fraction of the transient vacancies created at the initial stage of the construction of the crystal planes, however, are not annihilated during the time τ_i and are left behind the crystallization front. At temperatures close to T_m , when the velocity of the solidification front is relatively low and the vacancy mobility is high, i.e., $\tau_v < \tau_i$, the vacancies in a part of the crystal adjacent to the interface can move to and from the interface, leading to the establishment of a quasi-equilibrium vacancy concentration in the solidified material. As the level of undercooling increases, however, the interface velocity increases (Fig. 2a,b) while the vacancy mobility in the crystallized material decreases according to the Arrhenius temperature dependence, so that τ_v becomes comparable or greater than τ_i . Under these conditions, the vacancies left behind the crystallization front cannot escape to the liquid and are trapped in the crystallized material, creating a highly nonequilibrium vacancy concentration defined by the

kinetic processes at the crystallization front rather than the conditions of thermodynamic equilibrium at the temperature of crystallization.

At the qualitative level, the scenario described above is consistent with the temperature dependence of the vacancy concentration shown for Cr and Ni in Fig. 2c,d. The increase in the level of undercooling accelerates the propagation of the interface and leaves less time for atoms to migrate from liquid into the new crystal planes and to fill the vacant sites generated by the rapid construction of these planes occurring on the picosecond timescale. The decreasing temperature also reduces the rate of the thermally-activated atomic rearrangements at the interface. The combination of these two factors is likely to be responsible for the increase in the vacancy concentration with increasing undercooling observed in the whole range of temperatures for Ni (Fig. 2d) and for $0.8T_m < T < T_m$ for Cr. The decrease in the vacancy concentration at $T < 0.8T_m$ followed by a moderate increase at $T < 0.45T_m$ observed for Cr can be related to the slowdown in the interface velocity at low temperatures (Fig. 2a).

The translation of the qualitative physical picture outlined above into the design of an analytical model capable of quantitative description of the temperature dependences of vacancy concentration predicted in MD simulations, however, remains a challenge. Our attempt to adapt the existing models of vacancy generation [70–72], which treat the vacancy entrapment at the crystallization front in a manner similar to that of well-known solute trapping models, has not been successful. The non-Arrhenius temperature dependence of the atomic rearrangements responsible for the vacancy annihilation at the interface, as well as the lack of complete relaxation of the disordered phase in front of the rapidly advancing crystal-liquid interface [53,61,69] are likely to play an important role in defining the concentration of vacancies generated under conditions of strong undercooling.

3.3. Effect of interatomic interaction potential

In order to verify the general character of the temperature dependences of the vacancy concentration predicted in the MD simulations discussed above, we performed additional series of simulations of solidification in Ni crystal-liquid coexistence systems with (001) orientation of the crystal-liquid interfaces represented by the FBD [46], Mishin [47], and Bonny [48] EAM potentials. The lateral sizes of systems used in the simulations performed with Johnson [45], FBD [46], Mishin [47], and Bonny [48] EAM potentials are 28 nm, 5 nm, 28 nm, and 7 nm, respectively.

Before presenting the results of these simulations, we would like to note an important factor that has largely been ignored in the interpretation of predictions of earlier MD studies of crystallization under conditions of deep undercooling [52–57]. This factor is the onset of homogeneous nucleation of new crystallites inside the strongly undercooled liquid. As already mentioned above and illustrated in Fig. 1b, the homogeneous nucleation of small crystallites can significantly reduce the apparent velocity of the crystallization front at high levels of undercooling and can also affect the generation of crystal defects at the solidification front. The sensitivity of the kinetics of homogeneous crystallization predicted in the simulations to the choice of interatomic potential has been demonstrated [51], and is likely to be partially responsible for the variability of the crystallization front velocity trends predicted in the simulations. For example, a continuous decrease of the crystallization front velocity with increasing undercooling at $T < 0.6T_m$ predicted for FBD EAM Ni in Ref. [52] is different from the plateau extending down to $0.05T_m$ in Fig. 2b obtained for Johnson EAM Ni. It is demonstrated in Appendix A that this difference is, to a large extent, related to the homogeneous nucleation of new fcc crystallites inside the undercooled liquid, which is substantially more active

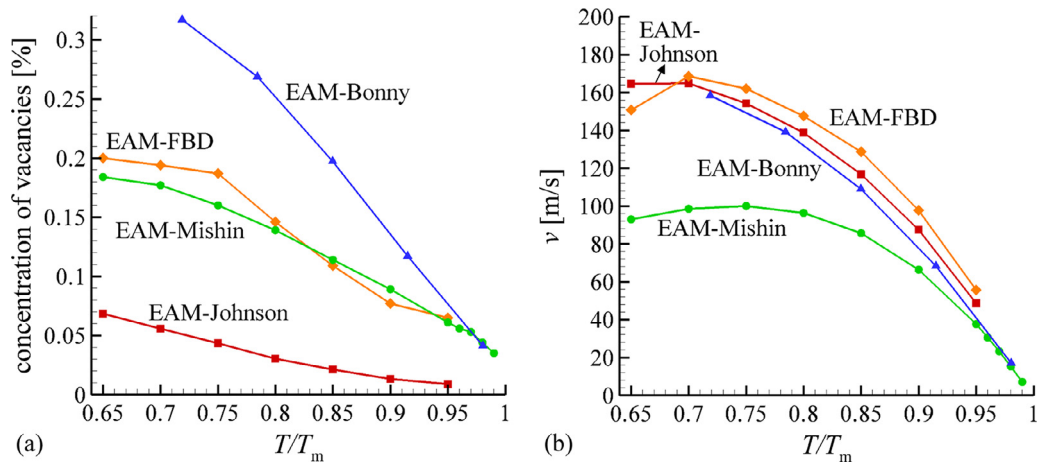


Fig. 4. The concentrations of vacancies in crystallized parts of crystal-liquid coexistence systems (a) and velocities of crystallization front (b) predicted in MD simulations of Ni coexistence systems with (001) orientation of the crystal-liquid interfaces described by Johnson [45], FBD [46], Mishin [47], and Bonny [48] EAM potentials.

in the simulations performed, for the same levels of undercooling, with the FBD EAM potential. The nucleation of new crystallites has also been reported for Bonny EAM Ni and Ni-based solid solution alloys undercooled below $0.7T_m$ [34]. Moreover, the formation of more exotic metastable phases is possible under conditions of rapid quenching, as exemplified in Appendix B by results obtained with Mishin EAM potential for Ni, which predicts the formation of Frank-Kasper σ -phase structure upon rapid quenching to $T < 0.65T_m$.

The onset of the rapid homogeneous crystallization predicted by some of the interatomic potentials for temperatures below $\sim 0.65T_m$ limits the range of temperatures where a reliable analysis of the vacancy generation at the crystallization front is possible with all four EAM potentials for Ni to $0.65T_m \leq T < T_m$. The results of the simulations are shown in Fig. 4. The crystallization front velocities predicted by four EAM potentials and shown in Fig. 4b exhibit similar increase with increasing degree of undercooling, although the velocities predicted by Mishin EAM potential at large undercoolings are noticeably smaller than those predicted by other three EAM potentials. The four temperature dependences of the vacancy concentration, shown in Fig. 4a, demonstrate larger quantitative differences, although all the dependences follow the same general trend of a continuous increase with increasing degree of undercooling. The common trend predicted with four different potentials demonstrates that the general mechanism of the vacancy generation at the crystallization front is not sensitive to the choice of the description of the interatomic interaction in a given material.

The substantial quantitative differences in the vacancy concentrations predicted by the four different potentials can partially be attributed to the differences in the vacancy formation energy at zero temperature, H_f^0 , predicted as 1.70 eV [73], 1.63 eV [46], 1.57 eV [47], and 1.48 eV [48] by Johnson, FBD, Mishin, and Bonny EAM potentials, respectively. When normalized by the values of the equilibrium melting temperature calculated for the corresponding potentials (see Section 2), the order of the normalized vacancy formation energies changes, with $H_f^0/k_B T_m$ ranging from 13.7 for Johnson, to 11.2 for Bonny, to 11.0 for FBD, and to 10.7 for Mishin potentials. The lowest level of the vacancy concentration obtained with Johnson EAM potential may indeed be related to the highest vacancy formation energy predicted by this potential, although the lack of obvious correlation between the normalized vacancy formation energy and the vacancy concentrations predicted with the other three potentials cautions against attributing the differences between the vacancy concentrations generated under conditions of

strong undercooling solely to the differences in the vacancy formation energy.

3.4. Effect of crystal-liquid interface orientation

The effect of crystallographic orientation of the crystal-liquid interface on the generation of vacancies during the crystallization front propagation is investigated for (001), (011), and (111) low-index interface orientations in Ni and Cr systems described by Mishin [47] and Johnson [21] EAM potentials, respectively. The range of temperatures considered in the simulations was limited to $T \geq 0.65T_m$ to avoid the effect of the homogeneous nucleation of new crystallites, discussed in Section 3.3 and Appendixes A and B, on the results of the simulations.

The results obtained for Ni and shown in Fig. 5 demonstrate that the dependences of crystallization front velocity and vacancy concentration on the level of undercooling obtained for different orientations of the interface follow the same general trends but exhibit large quantitative differences. Similarly to the dependences shown for different interatomic potentials and (001) interface in Figs. 2b,d and 4, for all three interface orientations, the vacancy concentrations exhibit a continuous increase with increasing undercooling (Fig. 5a), while the velocities of the interfaces reach the maximum values at $\sim 0.75T_m$ and stay at the high levels at lower temperatures (Fig. 5b).

The interface with (111) orientation represents a special case due to the emergence of growth twinning at temperatures below $0.9T_m$. The appearance of growth twinning below a threshold temperature of $0.87T_m$ is predicted for the (111) interface by theoretical analysis reported in Ref. [7] and is illustrated in Fig. 5c, where the coherent twin boundaries show up as green atomic planes connected by the incoherent twin boundaries shown in red. The onset of the growth twinning has a noticeable effect on the velocity of the crystallization front propagation, as can be seen by the deviation of the open diamonds for $T \leq 0.85T_m$ from the temperature dependence described by Eq. (1). It also complicates the evaluation of the vacancy concentration, which is done by counting the number of missing atoms in the crystallized region and accounts not only for single vacancies but also for vacancy clusters. With the onset of twinning, the incoherent twin boundaries start to make contribution to the apparent number of missing atoms, thus making the automatic counting of vacancies difficult. Counting of single vacancies is still possible after the onset of twinning with computational tools such as DXA, [74,75] but the concentration of single vacancies is about 20% lower than the totals plot-

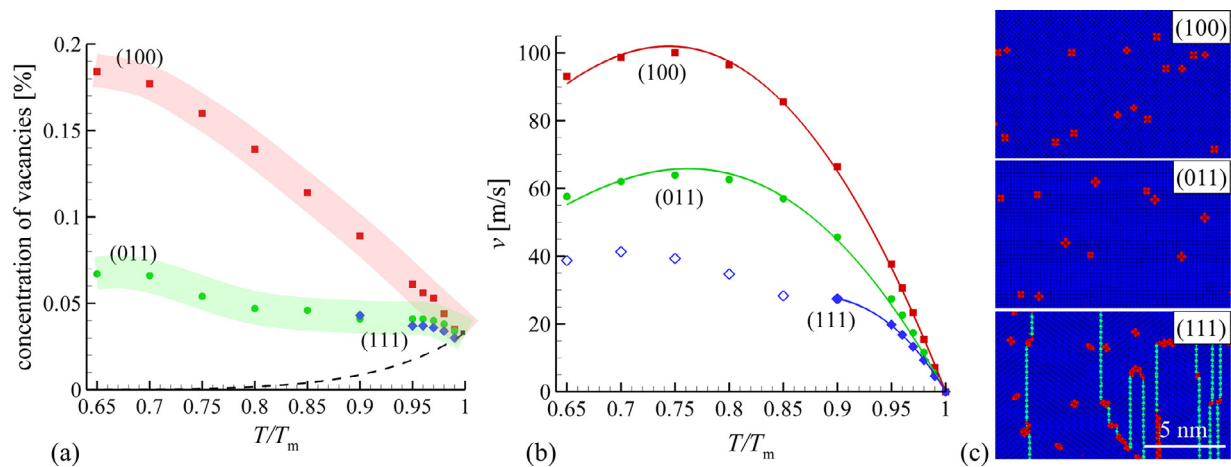


Fig. 5. The concentration of vacancies in crystallized parts of crystal-liquid coexistence systems (a) and velocities of crystallization front (b) predicted in MD simulations of Ni described by Mishin EAM potential [47]. The calculations are performed for three low-index orientations of solid-liquid interfaces, (001), (011), and (111). The error bars are comparable to the size of the symbols representing the data points and are not shown. The black triangle in (a) is the equilibrium concentration of vacancies at T_m predicted in an MD simulation, and the dashed line shows the theoretical equilibrium concentration of vacancies evaluated as described in Appendix C. The light red and green shaded areas in (a) serve as guidance to the eye and highlight the general trend in the temperature dependence of the vacancy concentration. In (b), the lines are the result of fitting of data points to Eq. (1), with parameters provided in Table 2. For (111) interface, only the data points at $T \geq 0.9T_m$, unaffected by growth twinning and shown by solid blue diamonds, are used in the fitting. The open diamonds show the velocity of (111) interface in the regime when the growth twinning is observed. The snapshots of small representative fragments of the three systems solidified at $T = 0.8T_m$ are shown in (c) to illustrate the onset of growth twinning in the (111) system. The atoms in the snapshots are colored according to their local structural environment, with blue, green and red colors used for atoms with local fcc, hcp, and undefined local structure. With this coloring scheme, a single green layer corresponds to a coherent twin boundary, while the red atoms are surrounding vacancies or belong to incoherent twin boundaries. The values of the vacancy concentration and crystallization front velocity shown in this figure are provided in Table S1 of the Supplementary Information.

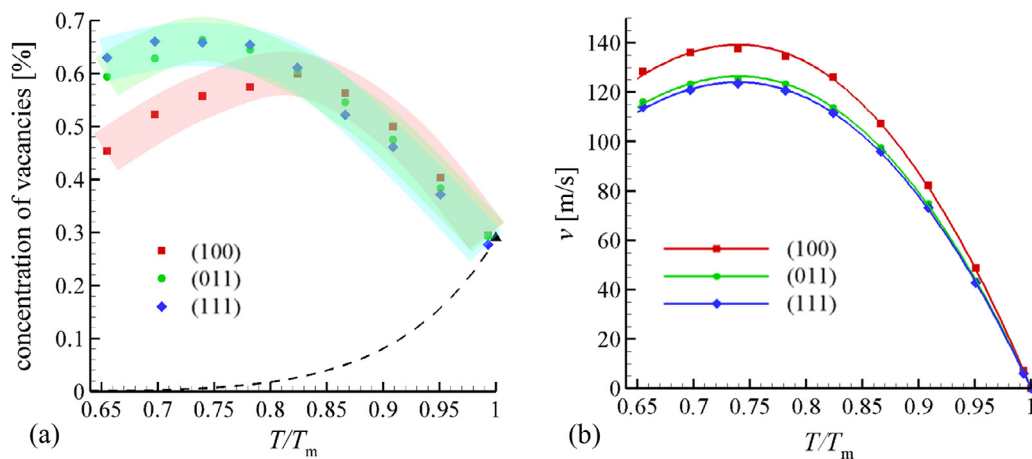


Fig. 6. The concentration of vacancies in crystallized parts of crystal-liquid coexistence systems (a) and velocities of crystallization front (b) predicted in MD simulations of Cr described by Johnson EAM potential [21]. The calculations are performed for three low-index orientations of the solid-liquid interface, (001), (011), and (111). The error bars in (a) are comparable to the size of the symbols representing the data points and are not shown. The black triangle in (a) is the equilibrium concentration of vacancies at T_m predicted in an MD simulation, and the dashed line shows the theoretical equilibrium concentration of vacancies evaluated as described in Appendix C. The light red, blue, and green shaded areas in (a) serve as guidance to the eye and highlight the general trend in the temperature dependence of the vacancy concentration. In (b), the lines are the result of fitting of data points to Eq. (1), with parameters provided in Table 2. The values of the vacancy concentration and crystallization front velocity shown in this figure are provided in Table S2 of the Supplementary Information.

ted in Fig. 5a. For example, the concentration of single vacancies generated in the propagation of (001) interface at $0.8T_m$ is 0.11%, while the total concentration of vacancies plotted for this interface in Fig. 5a is 0.14%. Therefore, while we list both the vacancy concentrations based on counting the single vacancies for $T \leq 0.95T_m$ and the ones based on automatic detection of all missing atoms for (111) interface in Table S1 of Supplementary Information, we only plot the total concentrations in Fig. 5a for $T \geq 0.90T_m$, where these values are reliable.

At the quantitative level, both vacancy concentration and velocity of the crystallization front propagation appear to be rather sensitive to the crystallographic orientation of crystal-liquid interface in Ni. In particular, at $T = 0.75T_m$, when the crystallization front velocities of (001) and (011) interfaces reach their maximum val-

ues, the velocity for (001) interface is about 56% higher than that of (011) interface. Note that the observation that the propagation of (001) interface is the fastest, and is followed by (011) and (111) interfaces, is consistent with earlier results of MD simulations reported for fcc metals [53,54,57,63,66].

The effect of the orientation of crystal-liquid interface on the vacancy generation and interface velocity in the bcc Cr system, illustrated in Fig. 6, is less pronounced as compared to the fcc Ni system. For all three interface orientations, the dependences of the vacancy concentration on the level of undercooling are very similar down to a temperature of $\sim 0.8T_m$, Fig. 6a. As the temperature decreases from $0.80T_m$ to $0.65T_m$, however, the vacancy concentration generated at the (001) interface decreases from $\sim 0.6\%$ to $\sim 0.45\%$, while the vacancy concentrations for (011) and (111) in-

Table 2

The parameters of Eq. (1) fitted to describe the dependence of the velocities of (001), (011), and (111) crystal-liquid interfaces on the level of undercooling in Ni and Cr systems described by Mishin [47] and Johnson [21] EAM potentials, respectively. With the exception of Ni (111) interface, the fitting is done for all data points between $0.65T_m$ and T_m . For Ni (111), only the data points at $T \geq 0.9T_m$, unaffected by growth twinning, are used in the fitting. The latent heat of melting calculated for these potentials is 0.187 eV/atom for Ni and 0.234 eV/atom for Cr.

	Ni (100)	Ni (011)	Ni (111)	Cr (100)	Cr (011)	Cr (111)
v_o^h , m/s	6450	6130	5550	9438	8604	8381
E_o^h , eV	0.340	0.382	0.400	0.470	0.471	0.470

terface orientations remain at or above the level of 0.6% down to $0.65T_m$.

As shown in Fig. 6b, the crystallization front velocity is higher for (001) interface orientation, although the difference with the other two orientations does not exceed 12%. The weak dependence of the crystallization velocity on the interface orientation is consistent with earlier study [53], where a much smaller difference in the interface velocities obtained for (100) and (110) orientations is reported for bcc metals as compared to fcc ones.

Similar to the results reported in Section 3.1, the temperature dependences of the crystallization front velocities predicted for the two materials and all three interface orientations are fitted to Eq. (1), with the fitting parameters listed in Table 2. The small difference between the parameters listed for Cr (001) interface in Tables 1 and 2 is related to the different ranges of data points used in the fitting. One can see that the Wilson-Frenkel expression provides a decent description of the MD results, although the dependences predicted in the simulations of Mishin EAM Ni, Fig. 5b, exhibit an apparent flattening at large undercooling, which is not captured by the Eq. (1). This flattening can be related to the transition to the extended plateau of velocities in the low temperature regime observed in Fig. 2b for Johnson EAM Ni (001) interface.

4. Summary

The generation of vacancies in the course of a rapid crystallization of metals is investigated in a series of MD simulations of crystal-liquid coexistence systems performed under well-controlled temperature and pressure conditions for two metals, bcc Cr and fcc Ni. The results of simulations performed for (001) orientation of the crystal-liquid interface reveal that, for both metals, the vacancy concentration in the parts of the coexistence systems crystallized through steady-state propagation of crystallization fronts exhibits a continuous increase with temperature decreasing down to $0.8T_m$, from a level close to the equilibrium vacancy concentration at $0.99T_m$ to 2–4 times higher vacancy concentrations at $0.8T_m$. At higher levels of undercooling, the vacancy concentration continues to increase with decreasing temperature for Ni and displays a nonmonotonous temperature dependence for Cr, where a decrease in the vacancy concentration down to a minimum at $\sim 0.5T_m$ is followed by a moderate rise upon further cooling.

The difference in the temperature dependences of the vacancy concentration observed for the two metals can be related to the qualitatively different trends in the temperature dependences of the crystallization front velocity. Following the initial increase to the maximum levels with temperature decreasing down to $\sim 0.75T_m$, the velocity of the crystal-liquid interface stays at an approximately constant level in a broad range of temperatures extending down to $0.05T_m$ in Ni, but gradually decreases down to zero in Cr. For neither Ni nor Cr, the temperature dependences of the crystallization front velocity predicted in the simulations can be described by any single theoretical kinetic equation suggested in literature for the crystallization process, although the Wilson-Frenkel equation that considers diffusional atomic rearrangements

at the crystal-liquid interface can be relatively well fitted to the data points in the temperature range from T_m down to $\sim 0.6T_m$.

The sensitivity of the computational predictions to the choice of interatomic potential is evaluated by performing simulations with four different versions of EAM potential for Ni. The general trend of increasing vacancy concentration with increasing level of undercooling is reproduced by all potentials, although the values of the vacancy concentration are significantly affected by the choice of the potential. Moreover, the propensity for homogeneous nucleation of new crystallites, including the formation of metastable crystal phases, under conditions of deep undercooling down to $\sim 0.65T_m$ and below is found to be highly sensitive to the choice of the interatomic potential. The onset of the rapid homogeneous crystallization predicted by most of the potentials limits the range of temperatures where a reliable analysis of the vacancy generation at the crystallization front is possible to $0.65T_m \leq T < T_m$.

The effect of crystallographic orientation of the crystal-liquid interface on the crystallization front velocity and generation of vacancies is also investigated by comparing the results obtained for (001), (011), and (111) interface orientations in Ni and Cr systems. In agreement with earlier studies, the velocity of solidification front in Ni is found to exhibit a strong orientation dependence, with the largest velocities observed for (001) interface, followed by (011) and (111) ones. For Cr, the order of the velocities is the same, but the orientation dependence is much weaker. The temperature dependences of the vacancy concentration follow the same trend for all orientations, and, similarly to the interface velocities, the quantitative differences in the vacancy concentrations are much more pronounced in Ni, where the vacancy concentration observed for (001) interface is more than twice higher than that for (011) at all temperatures below $0.9T_m$.

Given the sharp drop of the equilibrium vacancy concentration with decreasing temperature, the results of the simulations indicate that crystallization occurring under conditions of strong undercooling below the melting temperature can produce strong vacancy supersaturation exceeding the equilibrium levels of vacancy concentration at the corresponding temperatures by many orders of magnitude. This computational prediction has important implications for material processing techniques involving rapid localized melting and resolidification, as the generation of vacancy supersaturation may affect properties of resolidified regions by facilitating diffusional structural changes and phase transformations.

A detailed analysis of atomic-level rearrangements at the crystallization front is performed to get insights into the mechanisms responsible for the generation of the high vacancy concentrations in the rapid crystallization process. The movement of the crystal-liquid interface is found to proceed through the simultaneous construction of several atomic crystal planes, so that the interfacial layer consists of a quasi-two-dimensional mixture of disordered and crystalline regions. The disordered regions have lower density and serve as precursors for the vacancy formation. As a result, a large number of transient vacancies are created at the final stage of the rapid construction of the crystal planes. The absolute majority of these vacancies are quickly, within picoseconds, annihilated by the atomic flux coming from the liquid side of the interface. A small fraction of the vacancies created during the construction of the crystal planes, however, are not annihilated and are left behind the crystallization front. At low levels of undercooling, close to T_m , the velocity of the crystal-liquid interface is relatively low, the mobility of vacancies is high, and some of the excess vacancies trapped behind the crystallization front may diffuse to the interface and bring the vacancy concentration closer to the equilibrium level. As the undercooling increases, the faster movement of the interface and decreased vacancy mobility do not allow enough time for equilibration of the vacancy concentration in the newly built crystalline region, thus creating a strong vacancy supersaturation.

The generation of highly nonequilibrium vacancy concentration in this case is defined by the kinetic processes at the crystallization front rather than the conditions of thermodynamic equilibrium at the temperature of crystallization. Analysis of the temperature dependence of the atomic rearrangements occurring at the crystallization front suggests an important role of incomplete relaxation of the disordered phase at and in front of the crystal-liquid interface rapidly advancing under conditions of strong undercooling.

Declaration of Competing Interest

The authors declare that they have no known competing financial interests or personal relationships that could have appeared to influence the work reported in this paper.

Acknowledgments

Financial support for this work was provided by the U.S. Department of Energy, Office of Science, Basic Energy Sciences under contract number DE-SC0019191, as well as the DOE-supported Energy Frontier Research Center on the Energy Dissipation to Defect Evolution (DE-AC05-00OR22725). The authors thank Dr. Chengping Wu for calculation of the effective pair potential for Ni discussed in Appendix B. Computational support was provided by the National Science Foundation through the Extreme Science and Engineering Discovery Environment (project TG-DMR110090) and the University of Virginia Advanced Research Computing Services.

Appendix A. Homogeneous nucleation of new crystallites in FBD EAM Ni

The velocity of the crystallization front propagation and generation of vacancies in Ni are discussed in Sections 3.1 and 3.2 based on the results of MD simulations performed for (001) orientation of the crystal-liquid interface with Johnson EAM potential [45]. As shown in Fig. 2b, the solidification velocity predicted in the simulations increases with decreasing temperature up to a maximum level of ~ 170 m/s at $-0.7T_m$ and remains nearly constant with further reduction of temperature down to $0.1T_m$. A previous computational study of the temperature dependence of the (001) interface velocity in Ni [52] performed with FBD EAM potential [46], however, predicted a different behavior at strong undercoolings, with a continuous deceleration of the crystallization front with increasing undercooling below $0.6T_m$. In order to explain the difference in the computational results obtained with the two interatomic potentials, we repeated the small-scale (lateral dimensions of $5 \times 5 \text{ nm}^2$) simulations illustrated for Johnson EAM Ni in Fig. 2b by green diamonds with FBD EAM Ni potential.

The difference in the crystallization process predicted by the two potentials can be seen from the two series of snapshots of atomic configurations shown for each potential and temperatures of $0.6T_m$ and $0.3T_m$ in Fig. A1. The atoms in the snapshots are colored according to their local structural environment [76,77], so that fcc, bcc, and hcp crystal structures are light blue, dark blue, and green, respectively. All atoms that belong to the liquid phase or have an undefined local structural environment are blanked in order to expose all the crystalline regions. It is apparent from the snapshots that crystallization proceeds through two

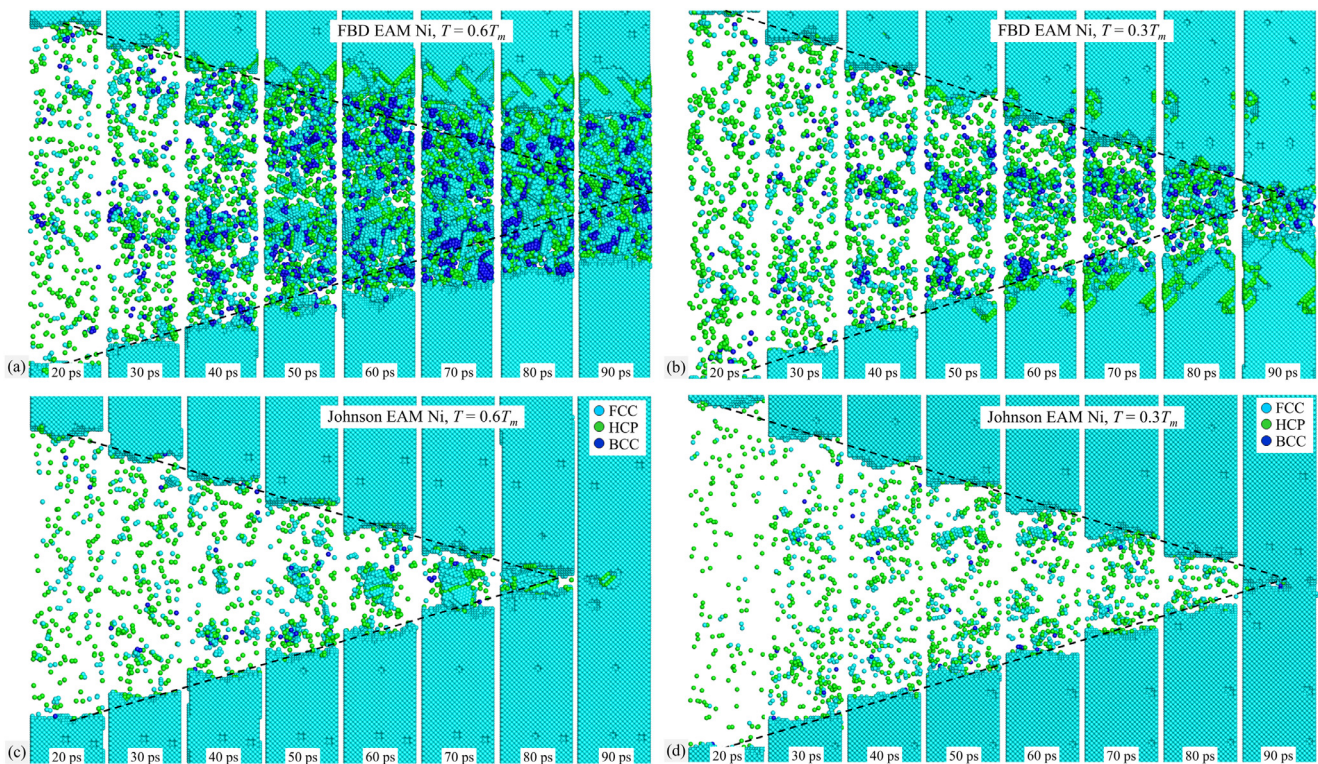


Fig. A1. Snapshots of the atomic configurations obtained in MD simulations of crystallization in Ni crystal-liquid coexistence systems with (001) orientation of crystal-liquid interfaces described by FBD EAM [46] (a,b) and Johnson EAM [45] (c,d) interatomic potentials. The simulations are performed at temperatures of $0.6T_m$ (a,c) and $0.3T_m$ (b,d). The snapshots are taken along the [010] view direction. The atomic configurations are quenched to 0 K for 1 ps to reduce thermal noise in atomic positions. The atoms are colored according to their local structure environment, with the light blue, dark blue and green colors corresponding to the fcc, bcc, and hcp structures, respectively. All the atoms that belong to the liquid phase or have an unknown local structural environment are blanked. The dashed lines show the approximate position of the crystallization fronts plotted under assumption that the initial crystallization front velocities are maintained throughout the simulations and are identical for the two crystallization fronts present in each system.

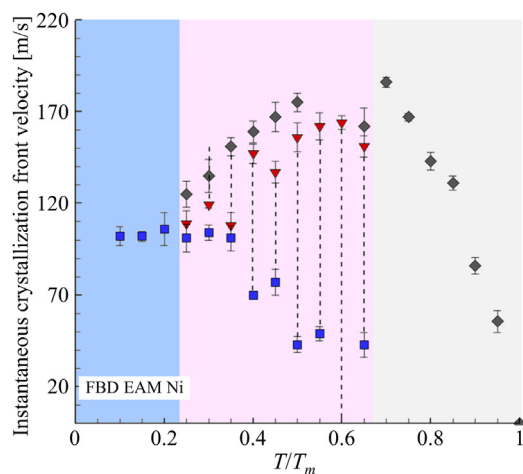


Fig. A2. Instantaneous velocities of the crystallization front predicted for different normalized temperatures in MD simulations of Ni crystal-liquid coexistence systems with (001) orientation of the crystal-liquid interfaces described by FBD EAM potential. The plot is divided into three regions shown with different background colors: the low-temperature and high-temperature regions where steady-state propagation of the crystallization fronts with time-independent velocities is observed are colored light blue and gray, respectively, while an intermediate region where the crystallization front velocity changes during the simulation is colored light pink. The gray diamonds show the crystallization front velocity that is not affected by the presence of crystalline nuclei generated in the undercooled liquid. The red nabla symbols represent the velocity of crystallization front at a time when the fraction of atoms with local crystalline surroundings inside the undercooled liquid reaches 3%. The blue square symbols represent the solidification front velocity during the last 10 ps of the simulation time. The error bars represent the standard deviation obtained from three series of MD simulations, each starting from a different initial configuration.

distinct processes: propagation of two crystallization fronts from the pre-existing crystalline region and homogeneous nucleation of new crystallites inside the disordered phase (undercooled liquid or glass). The homogeneous nucleation and growth of new crystallites is much more prominent in the FBD EAM Ni system, where the crystallites merge and form a continuous nanocrystalline region at $0.6T_m$ (Fig. A1a). The appearance and growth of the crystalline regions slows down and eventually halts the propagation of the two crystallization fronts in this simulation. Interestingly, at an even lower temperature of $0.3T_m$, the nucleation and growth of new crystallites is kinetically suppressed, which allows for the completion of crystallization through the propagation of two fronts eventually meeting each other in the middle of the system (Fig. A1b). Nevertheless, the homogeneous nucleation has a noticeable effect on the velocity of the crystallization fronts, as can be seen from a significant deviation of the position of the lower front from the dashed line which corresponds to the initial crystallization front velocity at the start of the crystallization process.

Overall, the snapshots shown for FBD EAM Ni demonstrate the difficulty of reliable evaluation of the velocity of crystallization front in the presence of active homogeneous nucleation and growth of new crystallites. This difficulty is further illustrated by Fig. A2, where the changes of the crystal-liquid interface velocity during the simulations are shown by the vertical dashed lines. In the part of the plot shown on the light pink background, the interface velocities are continuously decreasing as the fraction of crystalline phase generated through the homogeneous nucleation and growth of new crystallites increases.

The results shown for Johnson EAM Ni in Fig. A1c,d indicate that, while the homogeneous nucleation and growth of new crystallites takes place in these simulations as well, it does not prevent the steady state propagation of the two crystallization fronts, which do not significantly change their velocities during the sim-

ulation. Thus, we use this potential for the evaluation of the crystallization front propagation velocity in the broad range of temperatures (Fig. 2b), and limit the range of temperatures where the predictions obtained with four different potentials are compared in Section 3.3 to $0.65T_m \leq T < T_m$.

Appendix B. Generation of Frank Kasper σ -phase in Mishin EAM Ni

While EAM potentials have been highly successful in describing various properties of materials with metallic bonding, a substantial covalent contribution to bonding in transition metals makes it difficult to reproduce some of the properties affected by the directional nature of interatomic interactions. In particular, since ideal hcp and fcc structures have the same number of neighbors in the first and second nearest neighbor shells, as well as the same radii of the shells, the interaction with the third nearest neighbors should be sufficiently strong to distinguish between the two structures without introducing angular dependent components of the potential [78], which substantially increase the computational cost of simulations [79]. The ability to properly account for the contributions of third nearest neighbors is not only important for distinguishing the equilibrium fcc and hcp phases, but also for the ability to accurately reproduce experimental values of stacking fault and coherent twin boundary energies, which are important for simulations of plastic deformation of materials.

One of the ways to address this problem, proposed by Mishin and used in fitting of several interatomic potentials for Ni, Al, Ti, Ag, and Cu [47,80,81], is adding an oscillating component to the interatomic potential to amplify the contribution of the third nearest neighbor shell and reduce the contribution of the second nearest neighbor shell. The oscillatory nature of Mishin EAM potential for Ni [47] is illustrated in Fig. A3a, where the effective pair potential $\psi(r)$ is calculated using an approach suggested in Ref. [82], as $\psi(r) = \phi(r) + 2F'(\bar{\rho})f(r) + F''(\bar{\rho})[f(r)]^2$. In this equation, $\phi(r)$ is the two-body term, $f(r)$ is the electron density function, and $F(\bar{\rho})$ is the embedding function evaluated for a constant average electron density $\bar{\rho} = 0.9917$ that corresponds to fcc Ni equilibrated at 300 K. The oscillating shape of the effective pair interaction function, apparent from Fig. A3a, makes it possible to reproduce the nearly exact experimental values of stacking fault and twin boundary energies within the conventional EAM framework. At the same time, however, the oscillatory nature of the long-range part of the Mishin EAM potential also produces an unexpected side effect, which shows up under conditions of deep undercooling of liquid Ni.

In our analysis of the behavior of Mishin EAM Ni under conditions of deep undercooling we identified clear signs of a phase transformation when the liquid Ni is cooled to $0.6T_m$ and below. As can be seen from Fig. A3b, in the temperature range from T_m to $0.65T_m$ the coefficient of self-diffusion in the liquid phase Ni follows the Arrhenius temperature dependence, $D(T) = D_0 \exp(-E_b/k_B T)$ with an activation energy of $E_b = 0.683$ eV. As the temperature drops below $0.6T_m$, however, the diffusion coefficient experiences an abrupt drop, and the diffusion barrier changes to ~ 0.3 eV. This observation suggests a change in the structure of the material. A visual analysis of the system (left panel of Fig. A3d) also suggests the presence of an ordered structure. Nevertheless, a crystal structure analysis performed with popular tools, such as OVITO [83] and DXA [74,75], are unable to identify any common crystal structures in these systems.

To get insights into the structure of the phase generated from the undercooled molten Ni, we consider the radial distribution function depicted in Fig. A3e by the red curve. A notable characteristic of the radial distribution function is that the second peak is located at a distance of more than 4 \AA . Given the location of the

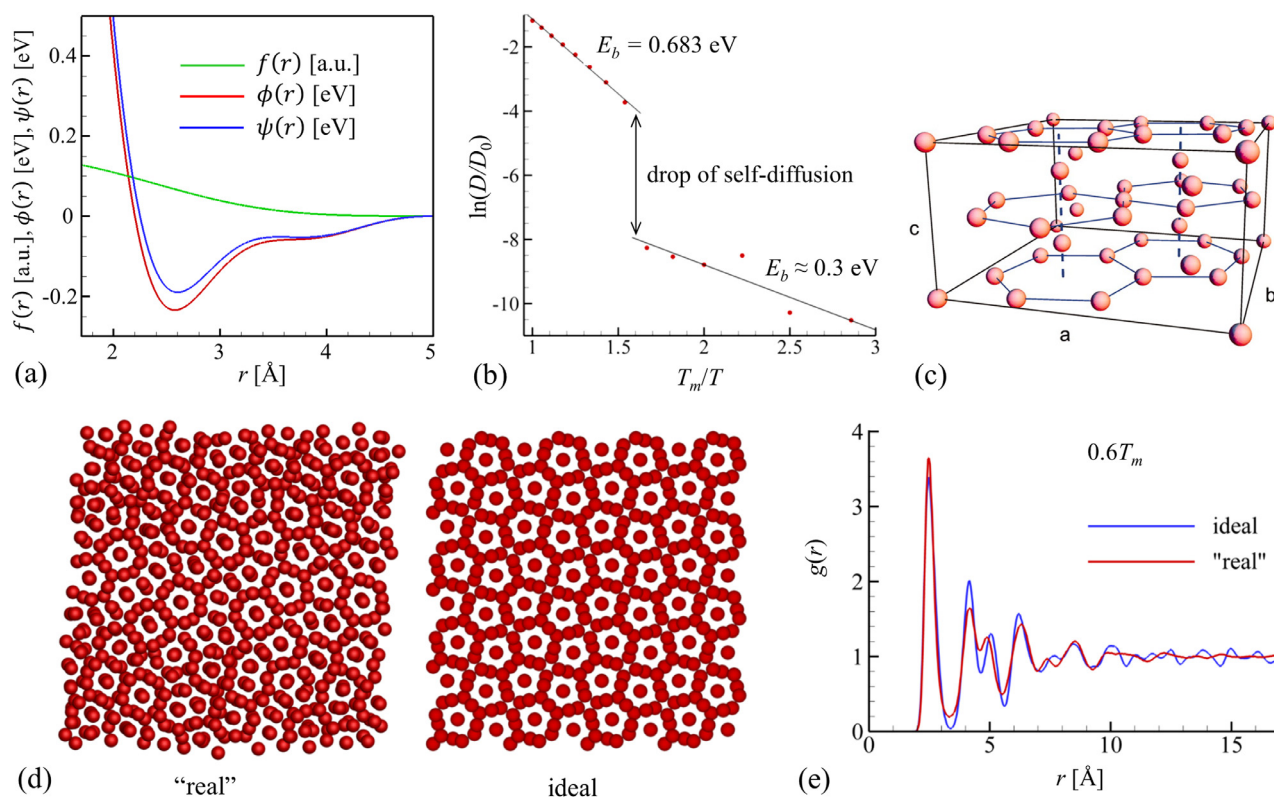


Fig. A3. Plots illustrating the generation of icosahedral Frank Kasper σ -phase in strongly undercooled Mishin EAM Ni. (a) The dependence of the two-body term $\phi(r)$ (red curve), the electron density function $f(r)$ (green curve), and the effective pair potential [82] $\psi(r)$ (blue curve) on interatomic distance r calculated with Mishin EAM Ni potential [47]. (b) Temperature dependence of self-diffusion coefficient predicted by this potential. (c) A unit cell of Frank Kasper σ -phase adapted from Ref. [84]. (d) Top view of a system generated in an undercooled Ni at $0.6T_m$ and quenched to zero temperature for 1 ps (left panel) and ideal Frank Kasper σ -phase shown with a view direction parallel to the c -axis (right panel). (e) The radial distribution function calculated for a system generated in undercooled Ni (red curve) and ideal Frank Kasper σ -phase (blue curve) computed at $0.6T_m$.

first peak at ~ 2.5 Å, the second peak can be expected at ~ 3.5 Å in fcc and hcp structures, and at 2.9 Å for bcc structure. This observation confirms that the low-temperature structure cannot be associated with common crystal phases characteristic of one-component metals. The large distance to the second neighbor shell, on the other hand, may suggest the icosahedral ordering of the structure. The structure closest to the one generated in the simulations appears to be the Frank Kasper (FK) σ -phase, as suggested by the similarity of the top views (along the c -axis of the FK unit cell, Fig. A3c) of the ideal FK structure with the one obtained in the simulation of liquid undercooled down to $0.6T_m$ shown in Fig. A3d, as well as by the comparison of the radial distribution functions shown for the two structures and the same temperature of $0.6T_m$ in Fig. A3e.

It has been demonstrated that the icosahedral local ordering, present in the FK σ -phase, can be induced and stabilized by specially designed interatomic pair potential exhibiting a strong oscillation at distances beyond the first neighbor shell [85,86]. Moreover, the formation of different icosahedral quasicrystal configurations in one-component systems composed of particles interacting with each other through oscillating pair potentials have recently been demonstrated in large-scale MD simulations [87,88]. These results suggest that the observation of the FK phase in the present simulations are related to the presence of oscillations in the Mishin EAM potential, which can be seen in Fig. A3a.

The comparison of cohesive energies calculated with three Ni potentials for the fcc, hcp, and FK σ -phase and listed in Table A1 shows that, indeed, the energy of the FK phase predicted by the Mishin EAM potential is lower than those predicted for this phase by the other two potentials. Nevertheless, the cohesive energy of

fcc is still lower than that of FK σ -phase, thus, suggesting that the generation of the icosahedral FK σ -phase structure is largely defined by kinetic factors. Indeed, the icosahedral ordering naturally emerges from local energy minimization and close packing of atoms in monoatomic disordered systems [89,90], and is commonly observed in MD simulations of undercooled liquids and metallic glasses [91–93]. Experimental confirmation of local icosahedral order in binary metallic glasses has also been reported [94]. The non-crystalline pentagonal symmetry inherent to icosahedrons and other extended tetrahedral clusters makes them incompatible with fcc crystal structure and contributes to the relative stability of the amorphous structure against the crystallization [91]. The energy barrier for the formation of FK σ -phase, which incorporates the icosahedral structural elements into the long-range crystal structure, can be expected to be reduced with respect to the fcc structure. Thus, under conditions when the energy of the metastable FK σ -phase is only slightly higher than that of the stable fcc phase, the formation of the former from the a strongly supercooled liquid is not surprising.

To sum up, an oscillating component of Mishin EAM Ni potential [47] introduced in lieu of explicit angular dependence to provide an accurate description of stacking fault and twin boundary energies also increases the relative stability of the icosahedral Frank Kasper σ -phase. As a result, rapid cooling to temperatures below $0.65T_m$ leads to the formation of a metastable FK σ -phase instead of the nucleation and growth of the equilibrium fcc phase observed in simulations discussed for FBD and Johnson potentials in Appendix A. Since the presence of neither FK phases nor other quasicrystal phases has been observed experimentally for single-component metals, the formation of FK σ -phase in simulations is

Table A1
The cohesive energy E_0 and atomic volume V_0 of Frank Kasper σ , fcc, and hcp phases.

	FK σ -phase		fcc		hcp	
	E_0 [eV]	V_0 [\AA^3]	E_0 [eV]	V_0 [\AA^3]	E_0 [eV]	V_0 [\AA^3]
Mishin EAM Ni	-4.4176	10.92	-4.4500	10.90	-4.4279	10.95
FBD EAM Ni	-4.3565	11.15	-4.4500	10.90	-4.4506	10.90
Johnson EAM Ni	-4.3666	11.21	-4.4500	10.90	-4.4307	10.99

likely to be a computational artifact related to the oscillating nature of the Mishin EAM Ni potential.

Appendix C. Calculation of the equilibrium vacancy concentration

In order to assess the levels of vacancy supersaturation produced by the rapid crystallization, the temperature dependence of the equilibrium values of vacancy concentration is calculated as

$$n_{eq} = \exp\left(-\frac{G_f(T)}{k_B T}\right), \quad (\text{A1})$$

where $G_f(T) = H_f(T) - TS_f(T)$ is the Gibbs free energy of the vacancy formation, $H_f(T)$ is the vacancy formation enthalpy, and $S_f(T)$ is the (vibrational) entropy associated with the vacancy formation. The temperature dependence of the vacancy formation enthalpy $H_f(T)$ in Ni and Cr described by Mishin [47] and Johnson [21] EAM potentials, respectively, is calculated in a series of constant temperature and constant (zero) pressure simulations, as the enthalpy difference between systems with and without a vacancy, i.e., $H_f = H^{(N-1)} - (N-1)H^{(N)}/N$, where $H^{(N)}$ and $H^{(N-1)}$ are the total enthalpies of systems with and without a vacancy, and N is the number of atoms in a defect-free system. The obtained tempera-

Table A2

Fitting parameters used in Eqs. (A2)-(A5) to describe the temperature dependence of the vacancy formation enthalpy, entropy, and free energy in EAM Ni and Cr crystals, as well as the equilibrium vacancy concentration at T_m determined in MD simulations.

	H_f^0 , eV	S_f^0 , k_B	A, eV/ K^2	B, eV	C, K	$n_{eq}(T_m)$
Ni	1.57	1.93	3.06×10^{-8}	306	12690	3.3×10^{-4}
Cr	2.01	2.94	3.33×10^{-8}	48.4	13140	2.9×10^{-3}

ture dependences of the enthalpy of vacancy formation are fitted to the following equation,

$$H_f(T) = H_f^0 + AT^2 + Be^{-C/T}, \quad (\text{A2})$$

as shown by the red lines in the left panels of Fig. A4. The fitting parameters H_f^0 , A, B, and C obtained for the two model materials are listed in Table A2. The temperature dependence of the entropy and free energy of the vacancy formation can then be expressed as

$$S_f(T) = -\left(\frac{\partial G_f}{\partial T}\right)_p, \quad G_f(T) = -T \int \frac{H_f(T)dT}{T^2}, \quad (\text{A3})$$

$$S_f(T) = S_f^0 + 2AT + B(T^{-1} + C^{-1})e^{-C/T}, \quad (\text{A4})$$

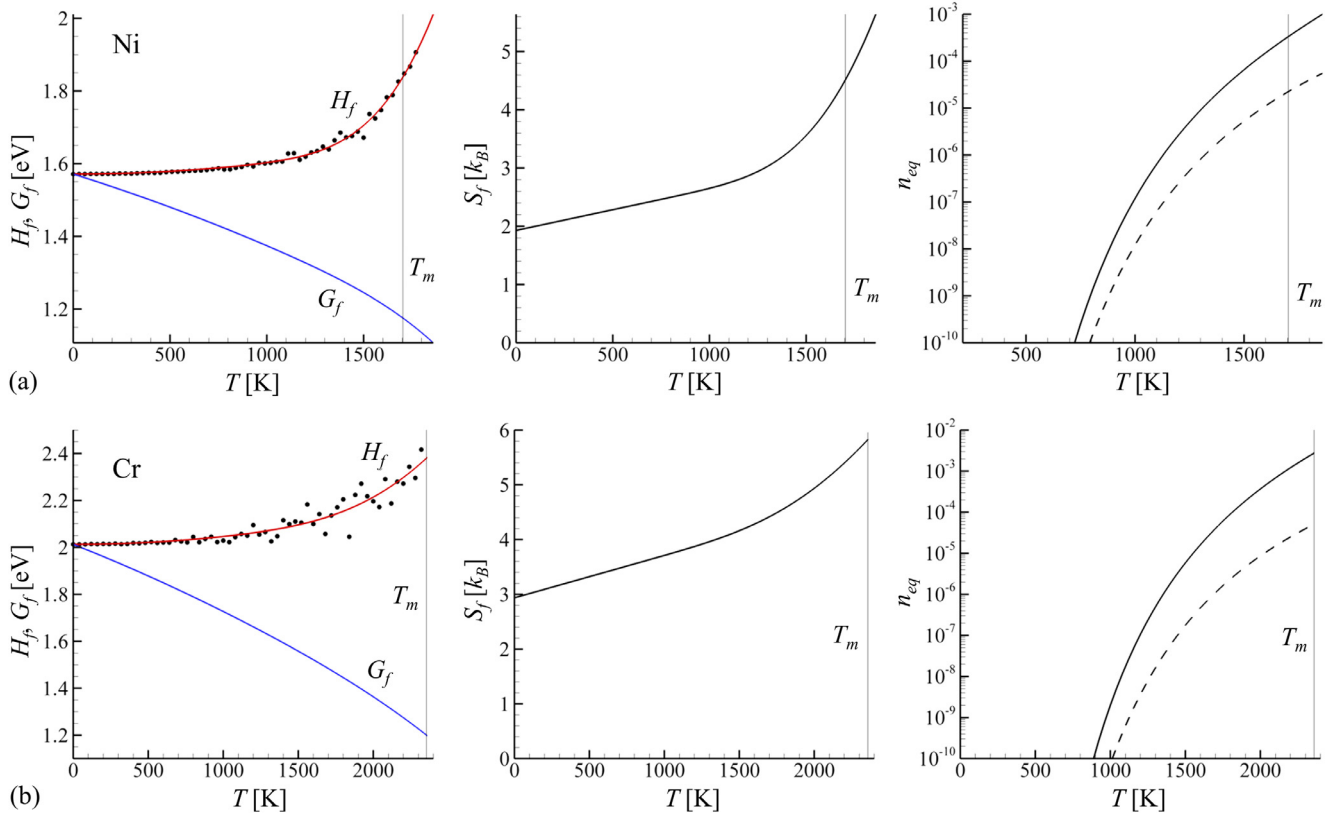


Fig. A4. The temperature dependences of enthalpy H_f , free energy G_f , entropy of vacancy formation S_f , and the equilibrium concentration of vacancies n_{eq} predicted for EAM Ni (a) and Cr (b) using Eqs. (A1)-(A5). The concentration of vacancies predicted with a constant value of the enthalpy of vacancy formation, $H_f = H_f^0$, and zero entropy of vacancy formation, $S_f = 0$, is shown by a dashed line in the right panels. The fitting parameters are listed in Table A2.

$$G_f(T) = H_f^0 - TS_f^0 - AT^2 - \frac{BT}{C} e^{-C/T}. \quad (\text{A5})$$

To obtain the parameter S_f^0 , which corresponds to the entropy of vacancy formation at 0 K, MD simulations are performed for crystalline systems representing free-standing films with thickness of 10 nm. The dimensions of the computational systems are $59 \times 59 \text{ nm}^2$ and $75 \times 75 \text{ nm}^2$ in the lateral (parallel to the free surfaces) directions for Cr and Ni, respectively, and periodic boundary conditions are applied in these directions. The initial vacancy concentrations of 0.4% and 0.08% are introduced in Cr and Ni systems, respectively, the systems are equilibrated at T_m , and constant temperature simulations are performed for up to 25 ns. The free surfaces of the films act as sources and sinks of the vacancies and, by the end of the simulations, the number of vacancies reaches the equilibrium value. In order to check the effect of the initial vacancy concentration, the simulation for Cr is repeated starting from system with zero vacancy concentration. The vacancy concentration is found to converge to the same equilibrium value. The equilibrium vacancy concentration, $n_{eq}(T_m)$, is then applied in Eq. (A1) along with $G_f(T_m)$ defined by Eq. (A5), and the parameter S_f^0 satisfying this equation at T_m is determined. The values of S_f^0 listed in Table A2, are comparable to those estimated for Ni and Cr in Ref. [95].

After all the parameters in Eq. (A2–A5) are determined, the equilibrium vacancy concentration is calculated as a function of temperature using Eq. (A1) and plotted in Fig. A4. The drop of the equilibrium vacancy concentration by many orders of magnitude with increasing undercooling is in a sharp contrast with the increase in the concentration of vacancies generated at the crystallization front, Figs. 2c,d, 4a, 5a, and 6a, indicating that extreme levels of vacancy supersaturation can be created by the rapid crystallization occurring under highly nonequilibrium conditions of deep undercooling. In the close vicinity of the melting temperature, where the velocity of solidification front is approaching zero and the mobility of vacancies is high, the vacancy concentrations generated in the crystallization process are approaching the equilibrium values at the equilibrium melting temperatures, shown by triangles in Figs. 2c, 5a, and 6a.

Supplementary material

Supplementary material associated with this article can be found, in the online version, at [10.1016/j.actamat.2020.11.007](https://doi.org/10.1016/j.actamat.2020.11.007).

References

- [1] R. Hellborg, H.J. Whitlow, Y. Zhang (Eds.), *Ion Beams in Nanoscience and Technology*, Springer-Verlag, Berlin, Heidelberg, 2009.
- [2] M.W. Ullah, D.S. Aidhy, Y. Zhang, W.J. Weber, Damage accumulation in ion-irradiated Ni-based concentrated solid-solution alloys, *Acta Mater.* 109 (2016) 17–22.
- [3] F. Granberg, K. Nordlund, M.W. Ullah, K. Jin, C. Lu, H. Bei, L.M. Wang, F. Djurabekova, W.J. Weber, Y. Zhang, Mechanism of radiation damage reduction in equiatomic multicomponent single phase alloys, *Phys. Rev. Lett.* 116 (2016) 135504.
- [4] A.A. Leino, G.D. Samolyuk, R. Sachan, F. Granberg, W.J. Weber, H. Bei, J. Liu, P. Zhai, Y. Zhang, GeV ion irradiation of NiFe and NiCo: Insights from MD simulations and experiments, *Acta Mater.* 151 (2018) 191–200.
- [5] Y. Zhang, T. Egami, W.J. Weber, Dissipation of radiation energy in concentrated solid-solution alloys: Unique defect properties and microstructural evolution, *MRS Bull.* 44 (10) (2019) 798–811.
- [6] C.-J. Lin, F. Spaepen, D. Turnbull, Picosecond pulsed laser-induced melting and glass formation in metals, *J. Non-Cryst. Solids* 61–62 (1984) 767–772.
- [7] X. Sedao, M.V. Shugaev, C. Wu, T. Douillard, C. Esnouf, C. Maurice, S. Reynaud, F. Pigeon, F. Garrelie, L.V. Zhigilei, J.-P. Colombarier, Growth twinning and generation of high-frequency surface nanostructures in ultrafast laser-induced transient melting and resolidification, *ACS Nano* 10 (2016) 6995–7007.
- [8] D.S. Ivanov, Z. Lin, B. Rethfeld, G.M. O'Connor, Th.J. Glynn, L.V. Zhigilei, Nanocrystalline structure of nanobump generated by localized photo-excitation of metal film, *J. Appl. Phys.* 107 (2010) 013519.
- [9] J. Ehrler, M. He, M.V. Shugaev, N.I. Polushkin, S. Wintz, V. Liersch, S. Cornelius, R. Hübner, K. Potzger, J. Lindner, J. Fassbender, A.A. Ünal, S. Valencia, F. Kronast, L.V. Zhigilei, R. Bali, Laser-rewritable ferromagnetism at thin-film surfaces, *ACS Appl. Mater. Interfaces* 10 (2018) 15232–15239.
- [10] W.H. Duff, L.V. Zhigilei, Computational study of cooling rates and recrystallization kinetics in short pulse laser quenching of metal targets, *J. Phys.: Conf. Ser.* 59 (2007) 413–417.
- [11] N.I. Polushkin, V. Oliveira, R. Vilar, M. He, M.V. Shugaev, L.V. Zhigilei, Phase-change magnetic memory: Rewritable ferromagnetism by laser quenching of chemical disorder in $\text{Fe}_{60}\text{Al}_{40}$ alloy, *Phys. Rev. Appl.* 10 (2018) 024023.
- [12] A.A. Martin, N.P. Calta, J.A. Hammons, S.A. Khairallah, M.H. Nielsen, R.M. Shuttlesworth, N. Sinclair, M.J. Matthews, J.R. Jeffries, T.M. Willey, J.R.I. Lee, Ultrafast dynamics of laser-metal interactions in additive manufacturing alloys captured by in situ X-ray imaging, *Mater. Today Adv.* 1 (2019) 100002.
- [13] C. Trautmann, Mirco- and nanoengineering with ion tracks, in: R. Hellborg, H.J. Whitlow, Y. Zhang (Eds.), *Ion Beams in Nanoscience and Technology*, Springer-Verlag, Berlin Heidelberg, 2009, pp. 369–387.
- [14] M.V. Shugaev, C. Wu, O. Armbruster, A. Naghilou, N. Brouwer, D.S. Ivanov, T.J.-Y. Derrien, N.M. Bulgakova, W. Kautek, B. Rethfeld, L.V. Zhigilei, Fundamentals of ultrafast laser-material interaction, *MRS Bull.* 41 (12) (2016) 960–968.
- [15] C. Wu, M.S. Christensen, J.-M. Savolainen, P. Balling, L.V. Zhigilei, Generation of sub-surface voids and a nanocrystalline surface layer in femtosecond laser irradiation of a single crystal Ag target, *Phys. Rev. B* 91 (2015) 035413.
- [16] W.-L. Chan, R.S. Averback, D.G. Cahill, Y. Ashkenazy, Solidification velocities in deeply undercooled silver, *Phys. Rev. Lett.* 102 (2009) 095701.
- [17] C.A. MacDonald, A.M. Malvezzi, F. Spaepen, Picosecond time-resolved measurements of crystallization in noble metals, *J. Appl. Phys.* 65 (1989) 129–136.
- [18] M.B. Agranat, S.I. Ashitkov, V.E. Fortov, A.V. Kirillin, A.V. Kostanovskii, S.I. Anisimov, P.S. Kondratenko, Use of optical anisotropy for study of ultrafast phase transformations at solid surfaces, *Appl. Phys. A: Mater. Sci. Process.* 69 (1999) 637–640.
- [19] J. Chen, W.-K. Chen, J. Tang, P.M. Rentzepis, Time-resolved structural dynamics of thin metal films heated with femtosecond optical pulses, *Proc. Natl. Acad. Sci. U. S. A.* 108 (2011) 18887–18892.
- [20] L.V. Zhigilei, Z. Lin, D.S. Ivanov, Atomistic modeling of short pulse laser ablation of metals: Connections between melting, spallation, and phase explosion, *J. Phys. Chem. C* 113 (2009) 11892–11906.
- [21] Z. Lin, R.A. Johnson, L.V. Zhigilei, Computational study of the generation of crystal defects in a bcc metal target irradiated by short laser pulses, *Phys. Rev. B* 77 (2008) 214108.
- [22] R. Vilar, Microstructure modification: Generation of crystal defects and phase transformations, in: K. Sugioka (Ed.), *Handbook of Laser Micro- and Nano-Engineering*, Springer, Cham, 2020.
- [23] A. Kumar, T.M. Pollock, Mapping of femtosecond laser-induced collateral damage by electron backscatter diffraction, *J. Appl. Phys.* 110 (2011) 083114.
- [24] X. Sedao, C. Maurice, F. Garrelie, J.-P. Colombarier, S. Reynaud, R. Quey, F. Pigeon, Influence of crystal orientation on the formation of femtosecond laser-induced periodic surface structures and lattice defects accumulation, *Appl. Phys. Lett.* 104 (2014) 171605.
- [25] M.P. Echlin, M.S. Titus, M. Straw, P. Gumbsch, T.M. Pollock, Materials response to glancing incidence femtosecond laser ablation, *Acta Mater.* 124 (2017) 37–46.
- [26] J.V. Oboña, V. Ocelík, J.C. Rao, J.Z.P. Skolski, G.R.B.E. Römer, A.J. Huis in 't Veld, J.Th.M. De Hosson, Modification of Cu surface with picosecond laser pulses, *Appl. Surf. Sci.* 303 (2014) 118–124.
- [27] C. Wu, L.V. Zhigilei, Nanocrystalline and polyicosahedral structure of a nanospike generated on metal surface irradiated by a single femtosecond laser pulse, *J. Phys. Chem. C* 120 (2016) 4438–4447.
- [28] M.V. Shugaev, C.-Y. Shih, E.T. Karim, C. Wu, L.V. Zhigilei, Generation of nanocrystalline surface layer in short pulse laser processing of metal targets under conditions of spatial confinement by solid or liquid overlayer, *Appl. Surf. Sci.* 417 (2017) 54–63.
- [29] C. Wu, E.T. Karim, A.N. Volkov, L.V. Zhigilei, Atomic movies of laser-induced structural and phase transformations from molecular dynamics simulations, in: M. Castillejo, P.M. Ossi, L.V. Zhigilei (Eds.), *Lasers in Materials Science*, Springer Series in Materials Science, 191, Springer International Publishing, Cham, Switzerland, 2014, pp. 67–100.
- [30] M.V. Shugaev, I. Gnilitzkiy, N.M. Bulgakova, L.V. Zhigilei, Mechanism of single-pulse ablative generation of laser-induced periodic surface structures, *Phys. Rev. B* 96 (2017) 205429.
- [31] C.-Y. Shih, I. Gnilitzkiy, M.V. Shugaev, E. Skoulas, E. Stratakis, L.V. Zhigilei, Effect of liquid environment on single-pulse generation of laser induced periodic surface structures and nanoparticles, *Nanoscale* 12 (2020) 7674–7687.
- [32] E.T. Karim, C. Wu, L.V. Zhigilei, Molecular dynamics simulations of laser-materials interactions: General and material-specific mechanisms of material removal and generation of crystal defects, in: V.P. Veiko, V.I. Konov (Eds.), *Fundamentals of Laser-Assisted Micro- and Nanotechnologies*, Springer Series in Materials Science, 195, Springer International Publishing, Cham, Switzerland, 2014, pp. 27–49.
- [33] E.T. Karim, Atomistic Simulation Study of Short Pulse Laser-Induced Generation of Crystal Defects in Metal Targets, PhD Dissertation (University of Virginia), 2016.
- [34] M. He, C. Wu, M.V. Shugaev, G.D. Samolyuk, L.V. Zhigilei, Computational study of short pulse laser induced generation of crystal defects in Ni-based single-phase binary solid solution alloys, *J. Phys. Chem. C* 123 (2019) 2202–2215.
- [35] P.T. Mannon, J. Magee, E. Coyne, G.M. O'Connor, T.J. Glynn, The effect of dam-

- age accumulation behavior on ablation thresholds and damage morphology in ultrafast laser micromachining of common metals in air, *Appl. Surf. Sci.* 233 (2004) 275–287.
- [36] J. Krüger, D. Dufft, R. Koter, A. Hertwig, Femtosecond laser-induced damage of gold films, *Appl. Surf. Sci.* 253 (2007) 7815–7819.
- [37] G. Raciukaitis, M. Brikas, P. Gecys, M. Gedvilas, Accumulation effects in laser ablation of metals with high-repetition-rate lasers, *Proc. SPIE* 7005 (2008) 70052L.
- [38] S.-N. Luo, T.J. Ahrens, Maximum superheating and undercooling: Systematics, molecular dynamics simulations, and dynamic experiments, *Phys. Rev. B* 68 (2003) 134206.
- [39] Z. Lin, E. Leveugle, E.M. Bringa, L.V. Zhigilei, Molecular dynamics simulation of laser melting of nanocrystalline Au, *J. Phys. Chem. C* 114 (2010) 5686–5699.
- [40] H.J.C. Berendsen, J.P.M. Postma, W.F. van Gunsteren, A. DiNola, J.R. Haak, Molecular dynamics with coupling to an external bath, *J. Chem. Phys.* 81 (1984) 3684–3690.
- [41] J. Monk, Y. Yang, M.I. Mendeleev, M. Asta, J.J. Hoyt, D.Y. Sun, Determination of the crystal-melt interface kinetic coefficient from molecular dynamics simulations, *Modelling Simul. Mater. Sci. Eng.* 18 (2010) 015004.
- [42] D.S. Ivanov, L.V. Zhigilei, Kinetic limit of heterogeneous melting in metals, *Phys. Rev. Lett.* 98 (2007) 195701.
- [43] S.I. Anisimov, B.L. Kapeliovich, T.L. Perel'man, Electron emission from metal surfaces exposed to ultrashort laser pulses, *Sov. Phys. - JETP* 39 (1974) 375–377.
- [44] D.S. Ivanov, L.V. Zhigilei, Combined atomistic-continuum modeling of short-pulse laser melting and disintegration of metal films, *Phys. Rev. B* 68 (2003) 064114.
- [45] X.W. Zhou, H.N.G. Wadley, R.A. Johnson, D.J. Larson, N. Tabat, A. Cerezo, A.K. Petford-Long, G.D.W. Smith, P.H. Clifton, R.L. Martens, T.F. Kelly, Atomic scale structure of sputtered metal multilayers, *Acta Mater.* 49 (2001) 4005–4015.
- [46] S.M. Foiles, M.I. Baskes, M.S. Daw, Embedded-atom-method functions for the fcc metals Cu, Ag, Au, Ni, Pd, Pt, and their alloys, *Phys. Rev. B* 33 (1986) 7983–7991.
- [47] Y. Mishin, Atomistic modeling of the γ and γ' -phases of the Ni-Al system, *Acta Mater.* 52 (2004) 1451–1467.
- [48] G. Bonny, D. Terentyev, R.C. Pasianot, S. Poncé, A. Bakaev, Interatomic potential to study plasticity in stainless steels: The FeNiCr model alloy, *Modelling Simul. Mater. Sci. Eng.* 19 (2011) 085008.
- [49] J. Rumble (Ed.), *CRC Handbook of Chemistry and Physics*, CRC Press, Boca Raton, 2016.
- [50] G.P. Purja Pun, Y. Mishin, Development of an interatomic potential for the Ni-Al system, *Philos. Mag.* 89 (2009) 3245–3267.
- [51] M.I. Mendeleev, M.J. Kramer, C.A. Becker, M. Asta, Analysis of semi-empirical interatomic potentials appropriate for simulation of crystalline and liquid Al and Cu, *Philos. Mag.* 88 (2008) 1723–1750.
- [52] Y. Ashkenazy, R.S. Averback, Atomic mechanisms controlling crystallization behavior in metals at deep undercooling, *EPL* 79 (2007) 26005.
- [53] Y. Ashkenazy, R.S. Averback, Kinetic stages in the crystallization of deeply undercooled body-centered-cubic and face-centered-cubic metals, *Acta Mater.* 58 (2010) 524–530.
- [54] T. Fang, L. Wang, Y. Qi, Molecular dynamics simulation of crystal growth of undercooled liquid Co, *Physica B* 423 (2013) 6–9.
- [55] L. Zhong, J. Wang, H. Sheng, Z. Zhang, S.X. Mao, Formation of monatomic metallic glasses through ultrafast liquid quenching, *Nature* 512 (2014) 177–180.
- [56] V.I. Mazhukin, A.V. Shapranov, M.M. Demin, N.A. Kozlovskaya, Temperature dependence of the kinetics rate of the melting and crystallization of aluminum, *Bull. Lebedev Phys. Inst.* 43 (2016) 283–286.
- [57] H.Y. Zhang, F. Liu, Y. Yang, D.Y. Sun, The molecular dynamics study of vacancy formation during solidification of pure metals, *Sci. Rep.* 7 (2017) 10241.
- [58] K.A. Jackson, B. Chalmers, Kinetics of solidification, *Can. J. Phys.* 34 (1956) 473–490.
- [59] F. Spaepen, D. Turnbull, Kinetics of motion of crystal - melt interfaces, *AlP Conf. Proc.* 50 (1979) 73–83.
- [60] K.A. Jackson, The interface kinetics of crystal growth processes, *Interface Sci* 10 (2002) 159–169.
- [61] P.K. Galenko, V. Anukudinov, Local non-equilibrium effect on the growth kinetics of crystals, *Acta Mater.* 168 (2019) 203–209.
- [62] L.V. Zhigilei, D.S. Ivanov, E. Leveugle, B. Sadigh, E.M. Bringa, Computer modeling of laser melting and spallation of metal targets, in: C.R. Phipps (Ed.), *High-Power Laser Ablation V*, 5448, *Proc. SPIE*, 2004, pp. 505–519.
- [63] J.J. Hoyt, B. Sadigh, M. Asta, S.M. Foiles, Kinetic phase field parameters for the Cu-Ni system derived from atomistic computations, *Acta Mater.* 47 (1999) 3181–3187.
- [64] F. Celestini, J.M. Debierre, Measuring kinetic coefficients by molecular dynamics simulation of zone melting, *Phys. Rev. E* 65 (2002) 041605.
- [65] J.J. Hoyt, M. Asta, Atomistic computation of liquid diffusivity, solid-liquid interfacial free energy, and kinetic coefficient in Au and Ag, *Phys. Rev. B* 65 (2002) 214106.
- [66] D.Y. Sun, M. Asta, J.J. Hoyt, Kinetic coefficient of Ni solid-liquid interfaces from molecular-dynamics simulations, *Phys. Rev. B* 69 (2004) 024108.
- [67] T. Egami, D. Srolovitz, Local structure fluctuations in amorphous and liquid metals: a simple theory of the glass transition, *J. Phys. F: Met. Phys.* 12 (1982) 2141–2163.
- [68] H.R. Wendt, F.F. Abraham, Empirical criterion for the glass transition region based on Monte Carlo simulations, *Phys. Rev. Lett.* 41 (1978) 1244–1246.
- [69] M.I. Mendeleev, Molecular dynamics simulation of solidification and devitrification in a one-component system, *Modell. Simul. Mater. Sci. Eng.* 20 (2012) 045014.
- [70] G.F. Bolling, D. Fainstein, On vacancy condensation and the origin of dislocations in growth from the melt, *Philos. Mag.* 25 (1972) 45–66.
- [71] C.DeW. Van Sicken, W.G. Wolfer, Nonequilibrium vacancy entrapment by rapid solidification, *Acta Metall. Mater.* 40 (1992) 2091–2100.
- [72] M. Hillert, M. Schwind, M. Selleby, Trapping of vacancies by rapid solidification, *Acta Mater.* 50 (2002) 3283–3291.
- [73] R.A. Johnson, Alloy models with the embedded-atom method, *Phys. Rev. B* 39 (1989) 12554–12559.
- [74] Dislocation Extraction Algorithm (DXA) tool, <http://ovito.org/dxa/download.html> (Accessed in January 2019).
- [75] A. Stukowski, K. Albe, Extracting dislocations and non-dislocation crystal defects from atomistic simulation data, *Modell. Simul. Mater. Sci. Eng.* 18 (2010) 085001.
- [76] G.J. Ackland, A.P. Jones, Applications of local crystal structure measures in experiment and simulation, *Phys. Rev. B* 73 (2006) 054104.
- [77] C. Wu, D.A. Thomas, Z. Lin, L.V. Zhigilei, Runaway lattice-mismatched interface in an atomistic simulation of femtosecond laser irradiation of Ag film - Cu substrate system, *Appl. Phys. A* 104 (2011) 781–792.
- [78] M.I. Baskes, R.A. Johnson, Modified embedded atom potentials for HCP metals, *Modell. Simul. Mater. Sci. Eng.* 2 (1994) 147–163.
- [79] S.J. Plimpton, A.P. Thompson, Computational aspects of many-body potentials, *MRS Bull.* 37 (2012) 513–521.
- [80] R.R. Zope, Y. Mishin, Interatomic potentials for atomistic simulations of the Ti-Al system, *Phys. Rev. B* 68 (2003) 024102.
- [81] P.L. Williams, Y. Mishin, J.C. Hamilton, An embedded-atom potential for the Cu-Ag system, *Modell. Simul. Mater. Sci. Eng.* 14 (2006) 817–833.
- [82] S.M. Foiles, Application of the embedded-atom method to liquid transition metals, *Phys. Rev. B* 32 (1985) 3409–3415.
- [83] Open Visualization Tool OVITO, <http://ovito.org/> (Accessed in January of 2017).
- [84] S. Lee, M.J. Bluemel, F.S. Bates, Discovery of a Frank-Kasper phase in sphere-forming block copolymer melts, *Science* 330 (2010) 349–353.
- [85] M. Dzugutov, Glass formation in a simple monatomic liquid with icosahedral inherent local order, *Phys. Rev. A* 46 (1992) R2984–R2987.
- [86] M. Dzugutov, Formation of a dodecahedral quasicrystalline phase in a simple monatomic liquid, *Phys. Rev. Lett.* 70 (1993) 2924–2927.
- [87] M. Engel, P.F. Damasceno, C.L. Phillips, S.C. Glotzer, Computational self-assembly of a one-component icosahedral quasicrystal, *Nat. Mater.* 14 (2014) 109–116.
- [88] P.F. Damasceno, S.C. Glotzer, M. Engel, Non-close-packed three-dimensional quasicrystals, *J. Phys.: Condens. Matter* 29 (2017) 234005.
- [89] F.C. Frank, Supercooling of liquids, *Proc. R. Soc. London Ser. A* 215 (1952) 43–46.
- [90] P.J. Steinhardt, D.R. Nelson, M. Ronchetti, Icosahedral bond orientational order in supercooled liquids, *Phys. Rev. Lett.* 47 (1981) 1297–1300.
- [91] V.A. Likhachev, A.I. Mikhailin, L.V. Zhigilei, Molecular dynamics study of medium-range order in metallic glasses, *Phil. Mag. A* 69 (1994) 421–436.
- [92] T. Tomida, T. Egami, Molecular-dynamics study of orientational order in liquids and glasses and its relation to the glass transition, *Phys. Rev. B* 52 (1995) 3290–3308.
- [93] J. Ding, E. Ma, Computational modeling sheds light on structural evolution in metallic glasses and supercooled liquids, *Npj Comput. Mater.* 3 (2017) 9.
- [94] A. Hirata, L.J. Kang, T. Fujita, B. Klumov, K. Matsue, M. Kotani, A.R. Yavari, M.W. Chen, Geometric frustration of icosahedron in metallic glasses, *Science* 341 (2013) 376–379.
- [95] J.J. Burton, Vacancy-formation entropy in cubic metals, *Phys. Rev. B* 5 (1972) 2948–2957.